UNIVERSITY OF CALIFORNIA SAN DIEGO

Ancient oceanic mantle below the Cascades inferred from the highly siderophile elements

A thesis submitted in partial satisfaction of the
requirements for the degree Master of Science

in

Earth Sciences

by

Ian Yuh

Committee in charge:

Professor James Day, Chair
Professor Geoffrey Cook
Professor Dave Stegman

2021

The thesis of Ian Yuh is approved, and it is acceptable

in quality and form for publication on microfilm and electronically.

University of California San Diego

2021

TABLE OF CONTENTS

Thesis Approval Page iii

Table of Contents iv

List of Supplementary Spreadsheets v

List of Figures vi

Acknowledgements viii

Abstract of the Thesis ix

1. Introduction 1

2. Samples and Methods 4

   2.1. Major- and trace-element abundance analysis 4
   2.2. Electron probe microanalyses (EPMA) 5
   2.3. Osmium and highly siderophile element analyses 6

3. Results 7

   3.1. Major element abundances 7
   3.2. Trace element variations 12
   3.3. Highly siderophile element (HSE) abundances and osmium isotope systematics 17
   3.4. Electron probe microanalysis results 19
   3.5. Geothermometry and oxygen fugacity 20

4. Discussion 21

   4.1. Lorena Butte volcanic stratigraphy and melt chemistry 21
   4.2. Melt infiltration in harzburgite xenoliths 26
   4.3. Melt depletion in harzburgite xenoliths 27
   4.4. Oxidation state 28
   4.5. Lorena Butte harzburgites: origin as mantle residuum below spreading ridge 30

5. Conclusions 31

6. Future Work 32

7. References 33

LIST OF SUPPLEMENTAL SPREADSHEETS

1. File Name: yuh_lorena_butte.xlsx

    Table 1: Major and trace element data for Lorena Butte and Blockhouse Butte trachybasalts

    Table 2: Major and trace element data for Lorena Butte harzburgite and crustal xenoliths

    Table 3: HSE abundance (ppb) and Os isotope data for Lorena Butte harzburgite xenoliths and a trachybasalt

    Table 4: Averaged EPMA major element abundances for Lorena Butte harzburgite olivine, spinel, orthopyroxene, and clinopyroxene (in wt.%)

    Table S1: Standard Reference Materials used for trace element abundance analyses (values in ppm)

    Table S2: EPMA analyses of olivine grains in Lorena Butte harzburgite xenoliths

    Table S3: EPMA analyses of orthopyroxene grains in Lorena Butte harzburgite xenoliths

    Table S4: EPMA analyses of clinopyroxene grains in Lorena Butte harzburgite xenoliths

    Table S5: EPMA analyses of spinel grains in Lorena Butte harzburgite xenoliths

    Table S6: Geothermometry and oxygen fugacity calculations

    Table S7: EPMA standards run with olivine

    Table S8: EPMA standards run with pyroxene

    Table S9: EPMA standards run with spinel

LIST OF FIGURES

Figure 1: Tectonic setting of the study is within the Cascade arc. The Simcoe Mountains volcanic field lies in southern Washington just east of the Cascade arc axis, which is approximated by a line running north to south connecting the chain of stratovolcanoes and volcanic centers, marked by red triangles. Dotted area denotes the Simcoe Mountains 3

Figure 2: Total alkali versus silica plot of volcanic rocks from Lorena Butte (red triangle), Blockhouse Butte (yellow upside-down triangle), and Simcoe Mountains volcanic field (blue circles). Volcanic rock fields are after Best (2003). Simcoe data are from Hildreth and Fierstein (2015). Transparency setting for data symbology is set to 20% for the Lorena and 8

Figure 3: Major elements versus MgO variation diagrams for volcanic rocks. Lorena Butte and Blockhouse Butte data from this study; Simcoe data from Hildreth and Fierstein (2015). Data symbology and transparency setting follow Figure 2. 9

Figure 4: Major elements versus SiO_2 variation diagrams for volcanic rocks. Lorena Butte and Blockhouse Butte data from this study; Simcoe data from Hildreth and Fierstein (2015. Data symbology and transparency setting follow Figure 2. 10

Figure 5: Major elements versus MgO for Lorena Butte harzburgites from this study and Brandon and Draper (1996) represented by green squares and blue pentagons, respectively, with 20% transparency. For comparison, abyssal harzburgites from Day et al. (2017) are plotted as grey diamonds with 50% transparency. 11

Figure 6: Lorena Butte harzburgites and trachybasalts whole-rock incompatible trace element concentrations. The harzburgites follow the general inflection pattern of the trachybasalts, which is interpreted to reflect refertilization of the peridotites with the melt. PM normalizations from McDonough and Sun (1995).....13

Figure 7: Lorena Butte harzburgite xenoliths and trachybasalts whole-rock REE concentrations. PM normalizations from McDonough and Sun (1995). 14

Figure 8: Lorena Butte and Blockhouse Butte trachybasalt whole-rock incompatible trace element concentrations. The trachybasalt trends closely follow the OIB trend after Sun and McDonough (1989). PM normalizations from McDonough and Sun (1995). 15

Figure 9: Whole-rock incompatible trace element concentrations of Lorena Butte crustal xenoliths. Mafic granulite LB2020C follows the same trend as the trachybasalts, while rhyolitic sample LB2023 follows a different trend with variable enrichments or depletion in fluid-mobile elements and elevated REEs. PM normalizations from McDonough and Sun (1995).....16

Figure 10: Trachybasalts and crustal xenolith whole-rock REE concentrations. PM normalizations from McDonough and Sun (1995). 17

Figure 11: Lorena Butte harzburgite Os isotope systematics. Measured $^{187}Os/^{188}Os$ for this study (green squares) is lower that of Brandon et al. (1996; blue pentagons). Error bars as shown for

this study are generally smaller than symbol size, except for $^{187}Os/^{188}Os$ in LB2007X due to a less-than-ideal laboratory run. 18

Figure 12: Lorena Butte harzburgites and trachybasalt LB2012 HSE abundances. PM-normalization from Day et al. (2017), with the following PM HSE abundances: 0.3 ppb Re, 5.3 ppb Pd, 7.5 ppb Pt, 7.9 ppb Ru, 3.6 ppb Ir, 3.9 ppb Os. 19

Figure 13: Terrain map of the southern section of Simcoe Mountains volcanic field showing the locations of Lorena Butte and Blockhouse Butte. The shield-like edifice spans the northwestern quarter of the map. Scattered cones and vents likely associated with the shield are marked by triangles.....22

Figure 14: Simplified ~15-meter vertical section of Lorena Butte showing relative stratigraphic positioning of samples. The sample numbers shown are the last two digits of the tephra samples (e.g., sample #23 is LB2023L). Thicknesses of strata are approximate and not to scale. 23

Figure 15: Incompatible trace element trend of the Lorena Butte trachybasalts versus Steens and Imnaha members of the CRBG. The trend of the trachybasalts generally follow that of Steens and Imnaha basalts (from Day et al., 2021) with greater abundances in more incompatible elements, as expected with the higher degree of melting associated with flood-basaltic.....25

Figure 16: Highly siderophile element content of the Lorena Butte trachybasalt versus the Steens basalts and a single sample of the Imnaha basalts (Day et al., 2021). Decreasing HSE abundances from Upper Steens, Lower Steens, to Imnaha basalts can be explained by increased mixing with crustal components. The trachybasalt HSE trend generally follows that of the Imnaha basalt.....26

Figure 17: Highly siderophile element content of Lorena Butte harzburgites (green solid lines) and abyssal harzburgites (Day et al., 2017; dashed grey lines). Lorena Butte harzburgites generally follow the trend of abyssal peridotites expect for more depletion in the moderately incompatible Re and slightly incompatible Pd, suggesting a similar to slightly greater 28

ACKNOWLEDGEMENTS

I would like to thank James Day for his support as my adviser and as an instructor. Through this season of the pandemic, his guidance out in the field, in the lab, and in remote has proven to be invaluable.

I thank Geoff Cook for fueling my passion in geology and counseling me in my career path. His enthusiasm about the topic and genuine care for his students strongly influenced my career path.

I also thank Dave Stegman for his knowledge and support. His advice in class enrollment has really helped me to gain a fuller understanding of the geological sciences.

I would also like to thank Stanley Mertzman of Franklin and Marshall College for the XRF measurement, Minghua Ren of University of Nevada Las Vegas for the EMPA, Fred Davis of University of Minnesota Duluth for his help in stoichiometric calculations for geothermometry and oxygen fugacity, and Ron English of Bishop Red Rock for guiding us during our field work at Lorena Butte.

Finally, I am grateful for my wife, Allaina Yuh, for the sacrifices she has made in my pursuit of higher education and career opportunities. I cherish all the times we spent together and would not have gotten where I am right now without her unwavering support.

ABSTRACT OF THE THESIS

Ancient oceanic mantle below the Cascades inferred from the highly siderophile elements

by

Ian Yuh

Master of Science in Earth Sciences

University of California San Diego, 2021

Professor James Day, Chair

Abstract: Mantle harzburgite xenoliths from Lorena Butte, Simcoe Mountains volcanic field, Washington, are examined to infer processes occurring in the mantle wedge below the Cascade arc. Previous studies have characterized these xenoliths with radiogenic $^{187}Os/^{188}Os$ and high oxidation states, suggesting intermixing with a slab component with highly radiogenic

osmium. In this study, I report osmium isotope systematics and highly siderophile element (HSE: Os, Ir, Ru, Pt, Pd, Re) abundances from a new suite of xenoliths collected from Lorena Butte. These data are coupled with mineral analyses and whole-rock major- and trace-element abundances.

The new $^{187}Os/^{188}Os$ measurements for ten harzburgites average 0.1231 $\pm$20 and are less radiogenic than xenoliths previously reported from the same locality, while the new estimates of oxygen fugacity within the xenoliths agree with literature data. The Lorena Butte harzburgites resemble abyssal harzburgites in $^{187}Os/^{188}Os$, HSE abundance systematics, major element chemistry, and estimated extent of melt depletion. The host melt bears a strong intraplate-melt signature despite its proximity to the Cascade arc. These geochemical lines of evidence suggest that the harzburgites are less influenced by subduction-related processes than previously thought. I propose that they represent mantle residuum from the oceanic lithosphere which has been entrained into the mantle wedge, and that the host magma represents an intraplate melt related to the melt which formed the Columbia River flood basalts. This illustrates the complex petrogenesis of the sub-arc lithosphere below the Cascades and suggests that subduction zones can preserve unusually old and melt-depleted mantle derived from a non-subduction tectonic setting.

1. Introduction

Subduction zones are a factory in the production of new crustal material derived from mantle melting. Oxidizing fluids derived from subducted slabs interact with the mantle wedge and depress its melting temperature (e.g., Peacock, 1990; Grove et al., 2006; Benard et al., 2018), generating chemically distinctive partial melts (e.g., Pearce, 1983; Parkinson & Arculus, 1999) which are sampled by volcanic arcs throughout the ocean and along continental margins. However, relatively little is known about processes occurring in the mantle wedge and the nature of the mantle wedge itself above a subduction zone largely due to the scarcity of mantle wedge materials at the surface (Widom et al., 2003).

Mantle peridotite xenoliths from the Simcoe Mountains volcanic field, Washington, offer an exceptional window into the mantle wedge beneath a modern arc. These xenoliths extruded in Pliocene-Pleistocene alkalic melts just east of the modern Cascade arc axis and have been shown to display high oxidation states suggestive of arc-related processes (Brandon & Draper, 1996). Simcoe is notable for being one of the few localities globally where mantle peridotites in an active arc setting can be sampled at the surface (e.g., Parkinson & Arculus, 1998; Widom et al., 2003; Arai & Ishimaru, 2007). It is also unusual as one of several volcanic centers in the central Cascade-arc region which exhibits basaltic intraplate-type (i.e., ocean island basalt [OIB] in a continental setting) volcanism, lacking the depletion of high field strength elements (HFSEs: Nb, Ta, Ti, Zr, Hf) and the enrichment of large ion lithophile elements (LILEs: K, Rb, Sr, Cs, Ba) characteristic of most arc magmas (Leeman et al., 1990).

Current evidence suggests that the mantle wedge underlying the Cascade arc is composed of refractory peridotites which have been metasomatized with slab-derived fluids (Brandon & Draper, 1996) and with melts which are unrelated to subduction processes (Ertan & Leeman, 1996; 1999), but ambiguity regarding its origin and petrogenesis still exists. Although peridotite xenoliths below the Cascade arc have been previous examined for their Os isotope systematics (Brandon et al., 1996), they have not been fully characterized for highly siderophile element (HSE: Os, Ir, Ru, Pt, Pd, Re) abundances. This omission is significant because the HSE are robust tracers of processes occurring in the lithospheric mantle including melt extraction, refertilization or metasomatism, and crustal recycling (Reisberg & Luguet, 2016; Walker,

2016). Since the HSE strongly partition into metal or sulfide phases, they preserve evidence of processes not manifested in other isotope systems (e.g., He-O-Sr-Nd-Hf-Pb; Day et al., 2013) and are particularly powerful in peridotites due to the strong compatibilities of the HSE during mantle melting.

Here, a new suite of mantle peridotite xenoliths collected from Lorena Butte, an alkalic scoria cone in the southern section of Simcoe, are examined for highly siderophile element abundances and Os isotope systematics. These data are complemented with whole-rock major- and trace-element chemistry and mineral chemistry, in addition to the characterization of a suite of associated trachybasalts representing the host melt and two trachybasalts from Blockhouse Butte, another scoria cone ~15 km to the west-northwest of Lorena Butte. In this thesis I characterize processes occurring in the mantle wedge beneath the Cascades, constrain the composition of the slab-derived fluids, and infer the relationship of the peridotite xenoliths to volcanological processes that led to their exhumation.

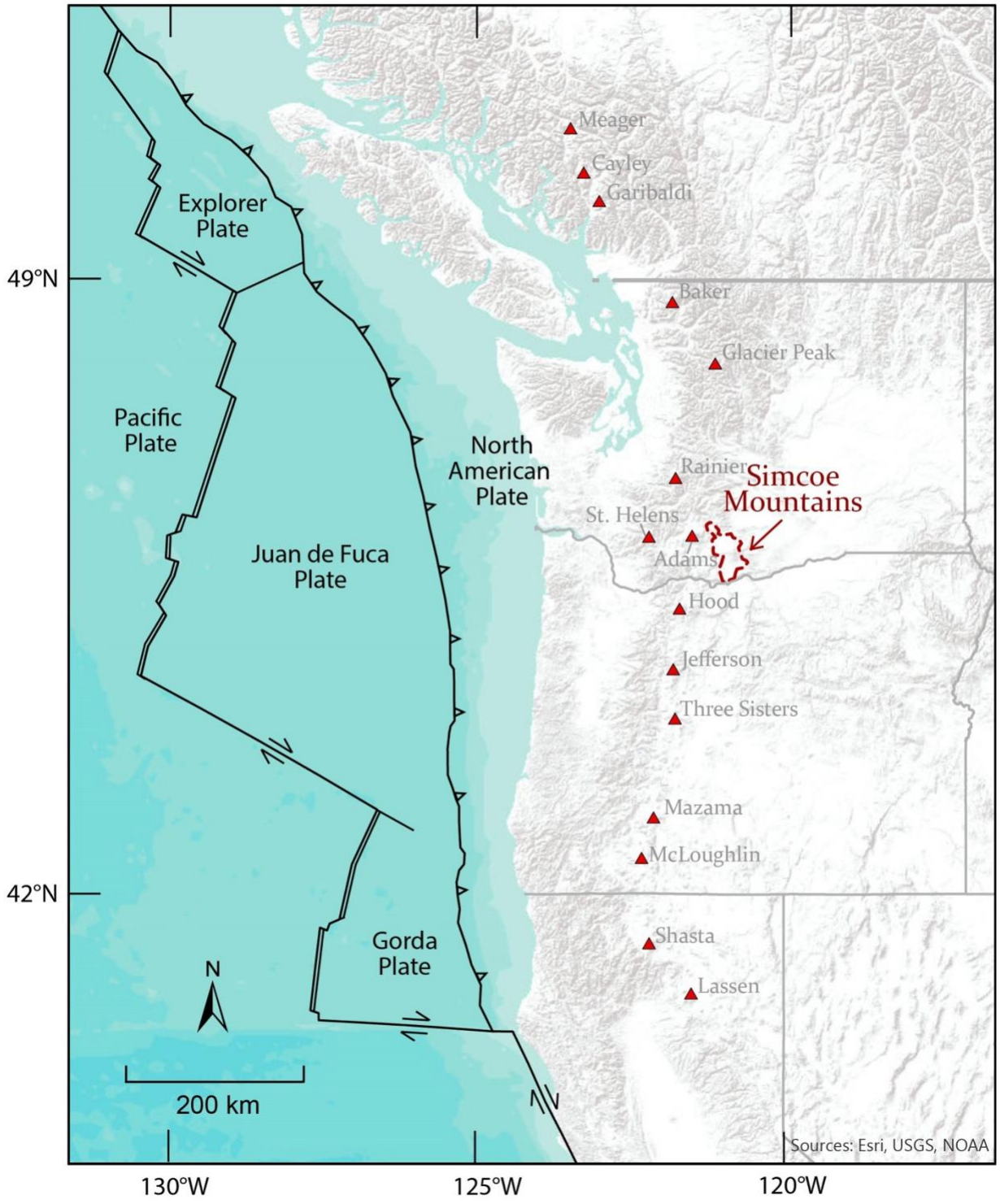

Figure 1: Tectonic setting of the study is within the Cascade arc. The Simcoe Mountains volcanic field lies in southern Washington just east of the Cascade arc axis, which is approximated by a line running north to south connecting the chain of stratovolcanoes and volcanic centers, marked by red triangles. Dotted area denotes the Simcoe Mountains volcanic field, modified after Hildreth and Fierstein (2015). Plate boundaries modified from ArcGIS layer by Pisut (2020) after Bird (2003).

2. Samples and Methods

In this study 11 spinel peridotite xenoliths, 16 trachybasaltic tephra representing host lavas, one trachybasaltic lava flow, and two crustal xenoliths taken from a larger subset of samples collected in the field were examined. The samples were collected during a field campaign that took place in October 2020, with the collection of tephra at Lorena Butte designed to examine if any variations in magma composition occurred during eruption. All samples were collected from Lorena Butte except for two trachybasalts collected at Blockhouse Butte. Eight of the studied tephra from Lorena Butte hosted peridotite xenoliths, and one hosted a crustal xenolith. All peridotite xenoliths collected in this study are harzburgites, although previous studies have also documented dunites, wehrlites, olivine-websterites, websterites, and olivine-orthopyroxenites in the Lorena Butte xenolith suite (Brandon & Draper, 1996; Ertan & Leeman, 1999). The samples were prepared by cutting into blocks using a diamond-tipped rotary saw, crushed using an alumina-plated jaw crusher, and powdered using an alumina shatter box.

2.1. Major- and trace-element abundances analyses

Whole-rock major element concentrations were done using X-ray fluorescence (XRF) analysis using a *PANalytical 2404* X-ray fluorescence vacuum spectrometer at Franklin and Marshall College, Lancaster, PA, following methods outlined in Boyd and Mertzman (1987) and Mertzman (2000). Samples were heated to determine loss on ignition (LOI) prior to the rock powder being mixed with lithium tetraborate, placed in a platinum crucible and heated with a Meker burner until molten. The molten material was then transferred to a platinum casting dish and quenched. This procedure produces a glass disk that is then used for XRF analysis. Typical accuracy of the analyses was ~1% for major elements for concentrations >0.5%. Major and minor elements in concentrations <0.5% had an accuracy of ~5%. Working curves for each element were determined by analyzing geochemical rock standards outlined in Abbey (1983), Govindaraju (1994), and Mertzman (2000). The compositions of Fe^{3+} and Fe^{2+} were calculated from the total measured FeO based on stoichiometry (Droop, 1987). Precision and accuracy are estimated using repeat analyses of standards, with long-term reproducibility (in wt. % and 2σ absolute

standard deviation, n = 13) of ±0.13 for SiO_2, ±0.01 for TiO_2, ±0.09 for Al_2O_3, ±0.63 for FeO, ±0.47 for Fe_2O_3, ±0.10 for $Fe_2O_3^T$, ±0.01 for MnO, ±0.04 for MgO, ±0.07 for CaO, ±0.03 for Na_2O, ±0.01 for K_2O, and ±<0.01 for P_2O_5. Accuracy for the average of 13 runs of BHVO-2 relative to USGS values is better than 0.2% for SiO_2 and TiO_2, <1% for Al_2O_3, MgO, $Fe_2O_3^T$, CaO, Na_2O, P_2O_5, and <3% for K_2O (Day et al., 2017). Elemental Rb, Sr, Zr, V, Cr, Ba were measured by both ICP-MS and XRF with generally 1:1 correlation (Table 1; Table 2), but ICP-MS measurements of these elements were preferred due to the higher sensitivity of the technique.

Whole-rock powders were measured for trace-element abundances at the SIGL. Samples were digested at 150°C in Optima grade concentrated HF (4 mL) and HNO_3 (1 mL) for >72 hrs on a hotplate with total analytical blanks and terrestrial basalt standards. Samples were sequentially dried and taken up in concentrated HNO_3 to remove fluorides, followed by dilution and doping with a 1 µg/g indium solution to monitor instrumental drift during analysis. Trace-element abundance analyses were done using a ThermoScientific iCAP Qc quadrupole ICP-MS in standard mode. Analyses were standardized versus reference material BHVO-2 that was measured throughout the analytical run. In addition, reference materials were analyzed as "unknowns" (BHVO-2, BIR-1, BCR-2, and AGV-2) to assess matrix matching, external reproducibility, and accuracy. For trace-elements, reproducibility of the reference materials was generally better than 5% (RSD), except for B (24% RSD), S (34% RSD), and Zn (10% RSD; Table S1). The reproducibility is in line with standard reference material data reported previously for the laboratory (e.g., Day et al., 2017).

2.2. Electron probe microanalysis (EPMA)

Polished thin sections were made for nine harzburgite xenoliths, and selected olivine, spinel, orthopyroxene, and minor clinopyroxene were analyzed for major- and minor-element compositions using a *JEOL* JXA-8900 electron probe microanalyzer equipped with four wavelength dispersive X-ray spectrometers at the University of Nevada Las Vegas. An acceleration potential of 15 kV and a beam current of 10 nA were used, with the beam focused to 2 μm. At least four separate spots for each mineral

phase were analyzed, except for clinopyroxene due to its low modal abundance in the harzburgites. Count times of 30 seconds (peak) and 15 seconds (background) were utilized for each element. Standards run with olivine, pyroxene, and spinel are listed in the Table S7, S8, S9, respectively.

2.3. Osmium and highly siderophile element analyses

Osmium isotope and the highly siderophile element (HSE) abundance analyses were performed at the *SIGL*. Precisely weighed homogenized powders were digested in sealed borosilicate Carius tubes with isotopically enriched spikes and a 1:2 mixture of Teflon distilled 10M HCl and 14M HNO_3 purged of excess Os by treatment and reaction with H_2O_2. Samples were digested in the oven at 270ºC for 72 hours. Osmium was triply extracted using CCl_4 then back-extracted into HBr (Cohen & Waters, 1996) before purification by a modified double micro-distillation procedure (Birck et al., 1997). The remaining HSE were recovered from the residual solution using standard anion exchange techniques (Day et al., 2016).

Osmium isotope compositions were measured using a *ThermoScientific* Triton thermal ionization mass spectrometer in negative mode (N-TIMS). Rhenium, Pd, Pt, Ru, and Ir were measured using a *Cetac* Aridus II desolvating nebulizer coupled to an iCAPQc ICP-MS. Offline corrections for Os involved an oxide correction, an iterative fractionation correction using $^{192}Os/^{188}Os = 3.08271$, a ^{190}Os spike subtraction, and finally, an Os blank subtraction. Precision for $^{187}Os/^{188}Os$, determined by measurement of the UMCP Johnson-Matthey standard run in the same magazines as samples was better than 0.2% (UMCP 35pg = 0.11377 ± 0.00025, n = 9). Rhenium, Ir, Pt, Pd and Ru isotopic ratios for sample solutions were corrected for mass fractionation using the deviation of the standard average run on the day over the natural ratio for the element. External reproducibility on HSE analyses was better than 0.5% for 0.5 ppb solutions and all reported values are blank corrected. The total procedural blank run with the samples had $^{187}Os/^{188}Os = 0.16 \pm 0.13$ with quantities (in picograms) of 20 [Re], 8 [Pd], 12 [Pt], 140 [Ru], 2.5 [Ir], and 0.25 [Os]. These blanks are similar to or slightly higher compared to those run recently in the laboratory (e.g., Snortum & Day, 2020) and relate either to the new batch of Carius tubes used, where the batch of Pyrex used can be a strong contaminant for the HSE (e.g., Day & Walker, 2015), or during minor cross-

contamination during column chemistry. Nonetheless, for most samples blank corrections were minor for Pd, Pt, and Ir at less than 2%, apart from Pt in LB2007X (88% blank contribution) and were below 8% for Ru except for LB2012L (58% blank contribution). Rhenium blank contributions ranged between 17 and 47%.

3. Results

3.1. Major element abundances

Major element variations in the Lorena Butte trachybasalts—scoriaceous tephra that host the xenoliths—span a relatively narrow range of MgO (5.23 to 6.74 wt. %), TiO_2 (2.16 to 2.31 wt. %), Al_2O_3 (16.0 to 16.8 wt. %), $Fe_2O_3^T$ (11.6 to 12.0 wt. %), CaO (6.3 to 6.6 wt. %), Na_2O (4.06 to 4.75 wt. %), and K_2O (2.15 to 2.39 wt. %), and have low loss on ignition (-0.2 to 1.1 wt. %). The two Blockhouse Butte trachybasalts—one tephra (BH2030L) and one lava flow (BH2032L)—have similar major element compositions, with MgO, TiO_2, and Na_2O in the field of Lorena Butte lavas within analytical uncertainty but slightly elevated CaO (6.84 wt. %) and lower K_2O (2.02 to 2.06 wt. %). Loss on ignition is similarly low (0.2 wt. %; Table 1).

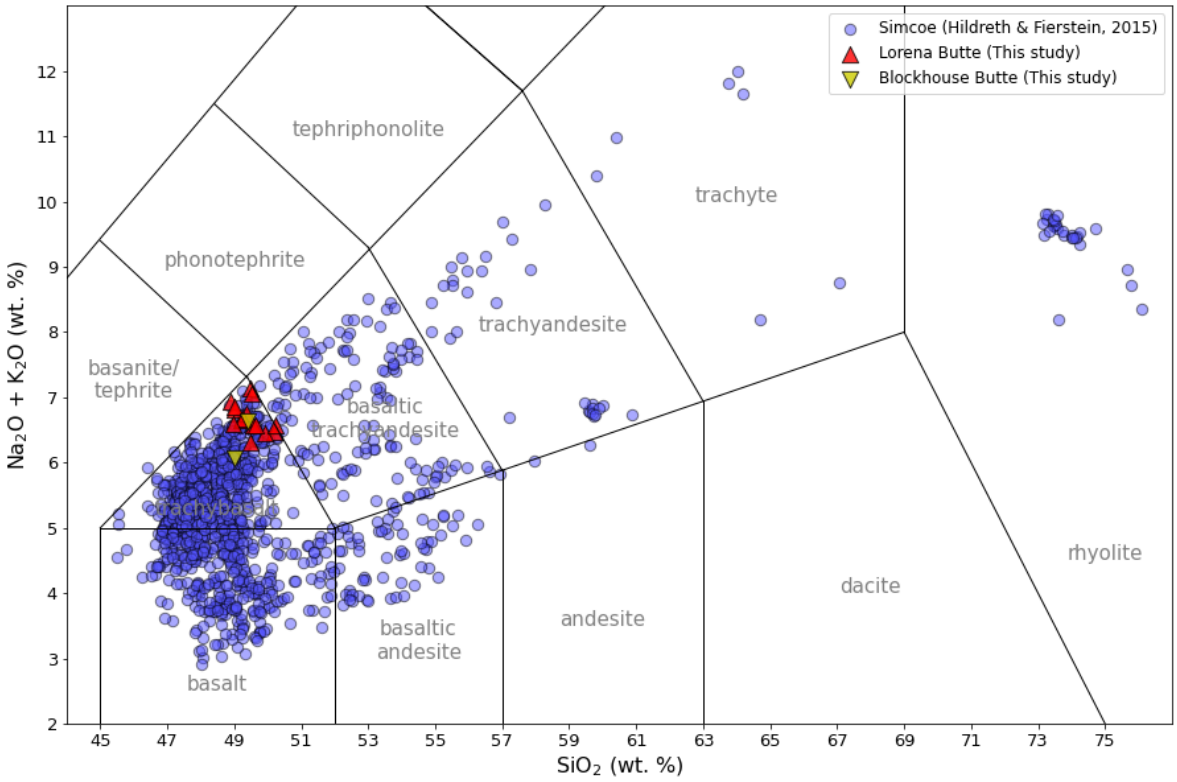

Figure 2: Total alkali versus silica plot of volcanic rocks from Lorena Butte (red triangle), Blockhouse Butte (yellow upside-down triangle), and Simcoe Mountains volcanic field (blue circles). Volcanic rock fields are after Best (2003). Simcoe data are from Hildreth and Fierstein (2015). Transparency setting for data symbology is set to 20% for the Lorena Butte and Blockhouse Butte data symbology and 50% for Simcoe data symbology to highlight overlapping data.

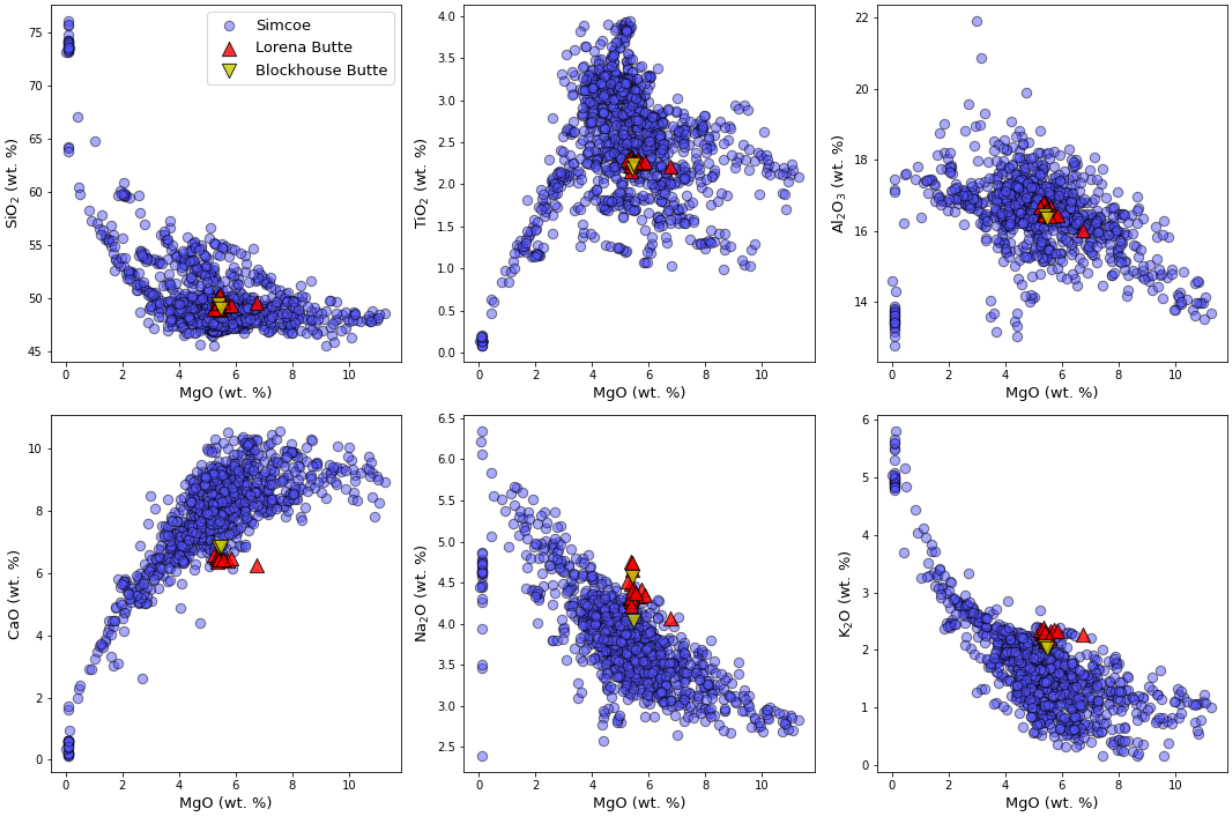

Figure 3: Major elements versus MgO variation diagrams for volcanic rocks. Lorena Butte and Blockhouse Butte data from this study; Simcoe data from Hildreth and Fierstein (2015). Data symbology and transparency setting follow Figure 2.

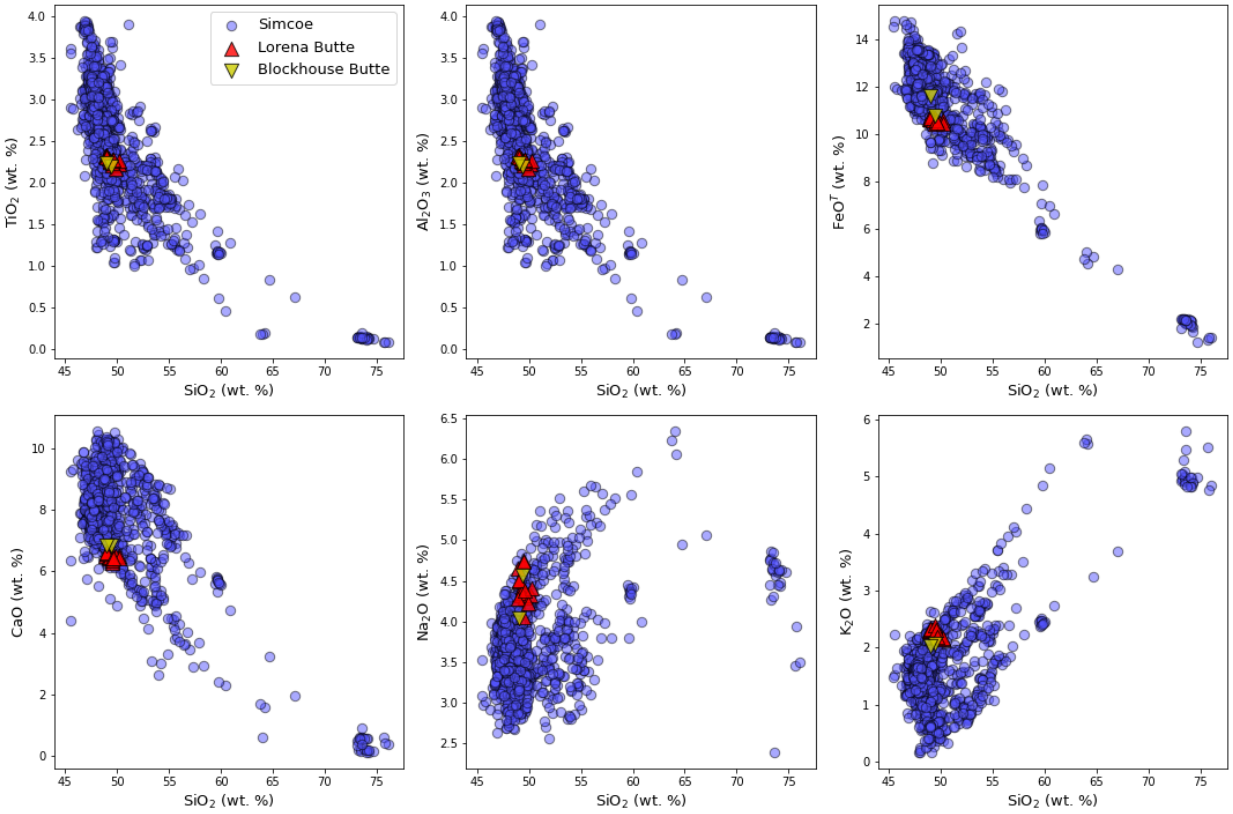

Figure 4: Major elements versus SiO_2 variation diagrams for volcanic rocks. Lorena Butte and Blockhouse Butte data from this study; Simcoe data from Hildreth and Fierstein (2015). Data symbology and transparency setting follow Figure 2.

Major element concentrations in the studied Lorena Butte harzburgite xenoliths are similar to those previously reported in the literature (Brandon & Draper, 1996) and to abyssal harzburgites (Day et al., 2017) and suggest that the harzburgites experienced significant melt depletion. The harzburgites span a range of MgO of 42.6 to 44.0 wt.%, Al_2O_3 of 0.98 to 2.46 wt. %, $Fe_2O_3^T$ of 8.22 to 9.94 wt. %, and CaO of 0.44 to 1.30 wt. %. Negative loss of ignition for the harzburgites (-0.6 to -0.1%) corresponds with visual evidence for little to no alteration in samples (Table 2).

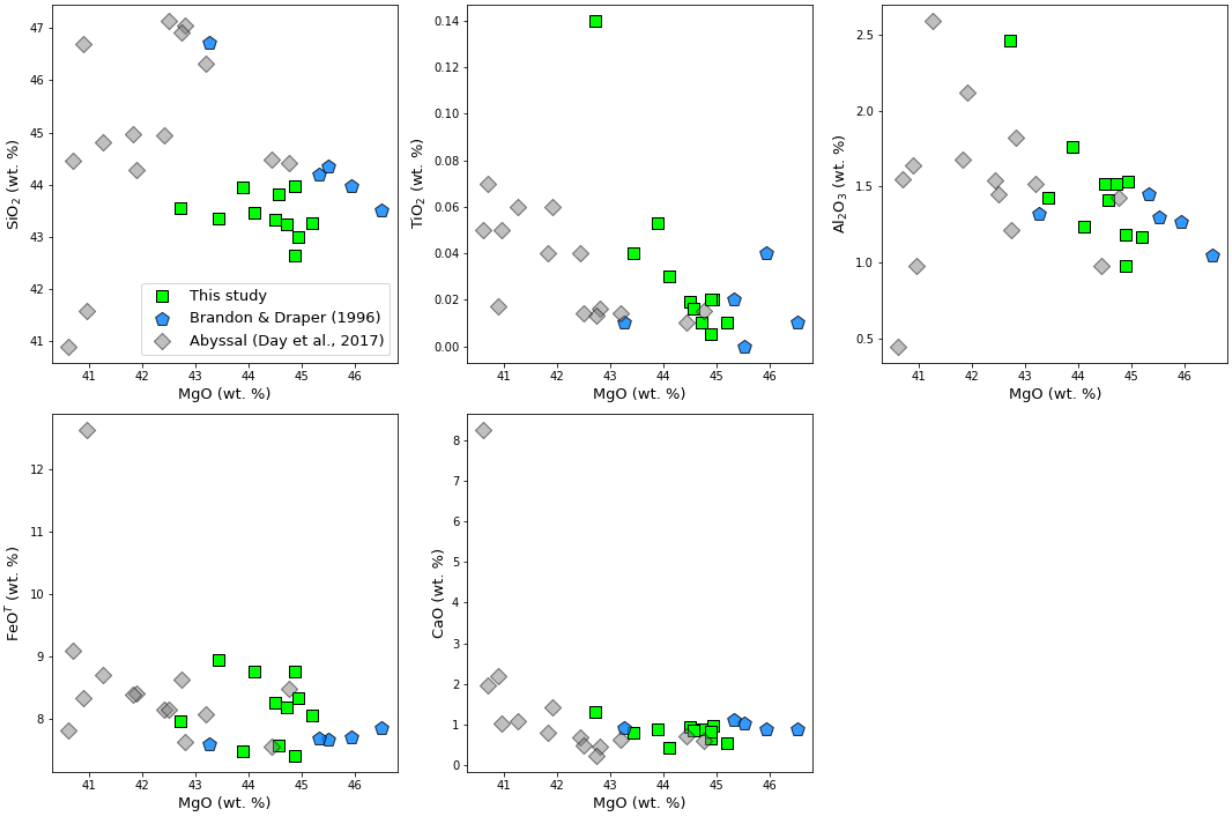

Figure 5: Major elements versus MgO for Lorena Butte harzburgites from this study and Brandon and Draper (1996), represented by green squares and blue pentagons, respectively, with 20% transparency. For comparison, abyssal harzburgites from Day et al. (2017) are plotted as grey diamonds with 50% transparency.

Major element variations in the two crustal xenolith samples differ considerably. Sample LB2020C—a mafic granulite—has major element abundances that closely match those of the lavas in MgO (5.41 wt. %), TiO_2 (2.12 wt. %), Al_2O_3 (16.0 wt. %), $Fe_2O_3^T$ (11.2 wt. %), CaO (6.37 wt. %), Na_2O (4.09 wt. %), and K_2O (2.18%). In contrast, sample LB2023C has elevated SiO_2 (82.9 wt. %) and low MgO (1.2 wt. %), TiO_2 (0.21 wt. %), Al_2O_3 (11.5 wt. %), $Fe_2O_3^T$ (1.56 wt. %), CaO (0.63 wt. %), Na_2O (0.99 wt. %), and K_2O (0.92 wt. %). Loss on ignition is 0.53 and 0.99 wt. %, respectively, for LB2020C and LB2023C (Table 1).

3.2. Trace element variations

In the trachybasaltic tephra, the incompatible trace elements range from ~4 × primitive mantle (PM; McDonough & Sun, 1995) abundances to ~100 × PM, with relative enrichment generally increasing with incompatibility. Exceptions to this trend are strong relative depletions in Cs and Pb in most samples, moderate relative depletions in Rb, Th, and U, and a slight relative enrichment in Sr. No relative depletion is observed for Nb and Ta, which suggests limited subduction influence on the lavas (Figure 6). The REE patterns display a narrow range of variation among samples and show a decreasing trend with increasing compatibility from La ~70 × PM to Lu ~4 × PM (Figure 7). The two Blockhouse Butte samples, though following the same trends, are generally slightly less enriched than those of Lorena Butte and show stronger depletions in Cs, U, and Pb (Figure 8).

The harzburgites have a high concentration of compatible trace elements (Cr 2260 to 4010 ppm, Ni 2270 to 2430 ppm, Co 113 to 130 ppm) relative to the trachybasalts (Cr 99 to 142 ppm, Ni 78.3 to 108 ppm, Co 31.7 to 39.5 ppm). For the harzburgites, the normalized abundances of incompatible trace elements range from ~0.02 × PM to ~10 × PM, and the plot is characterized by a sublinear trend just under PM concentration for the most incompatible elements, a slight decreasing trend for moderately incompatible elements, and an increasing trend for the least incompatible elements. The overall inflection pattern of the plot mirrors that of the trachybasalts. Trace elements displaying the most variability are Pb, U, K, Cs, Sr, Ba—generally large ion lithophile and/or fluid mobile elements. Harzburgite LB2007X displays an anomalously strong enrichment in K (5 × PM), whereas other harzburgites are at or below PM-values, and LB2015X is distinctively more enriched in rare earth elements (REEs) compared to other samples (Figure 6). The REE trend for the harzburgites generally displays a concave-up pattern, with light REE (LREE) just under 1 × PM, moderate REE (MREE) depletion of near 0.1 × PM, and a slight increase in heavy REE (HREE) relative to MREE (Figure 7).

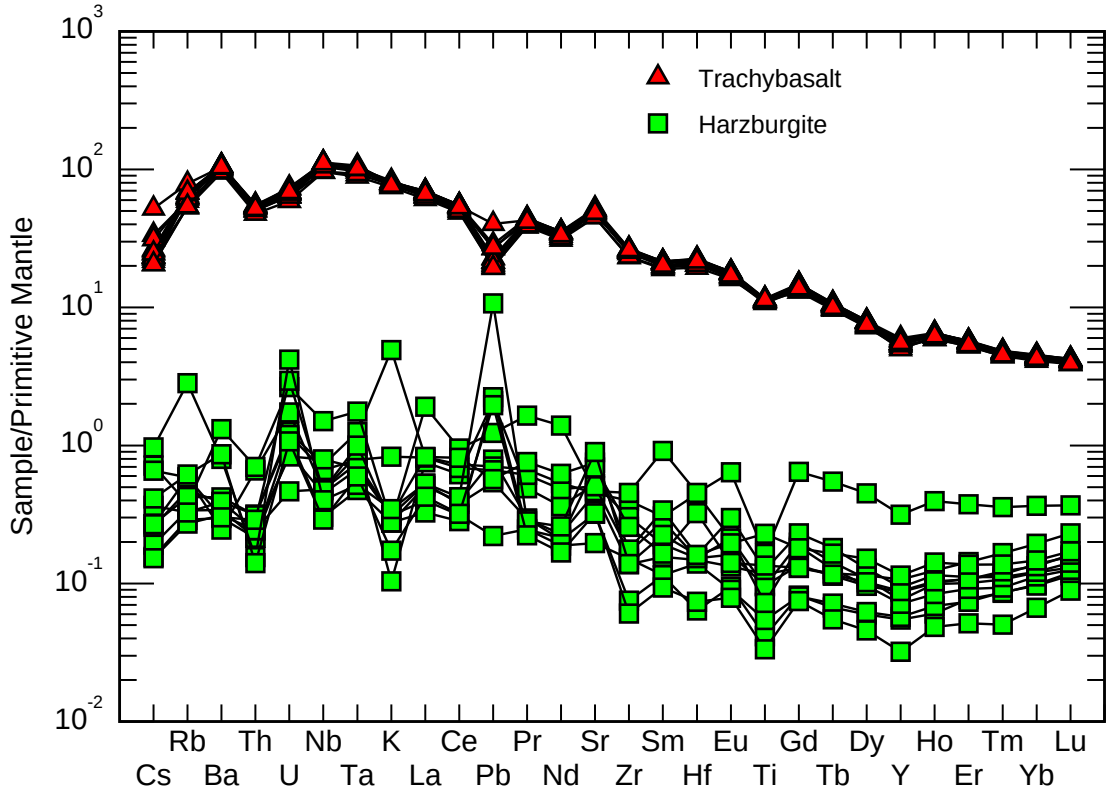

Figure 6: Lorena Butte harzburgites and trachybasalts whole-rock incompatible trace element concentrations. The harzburgites follow the general inflection pattern of the trachybasalts, which is interpreted to reflect refertilization of the peridotites with the melt. PM normalizations from McDonough and Sun (1995).

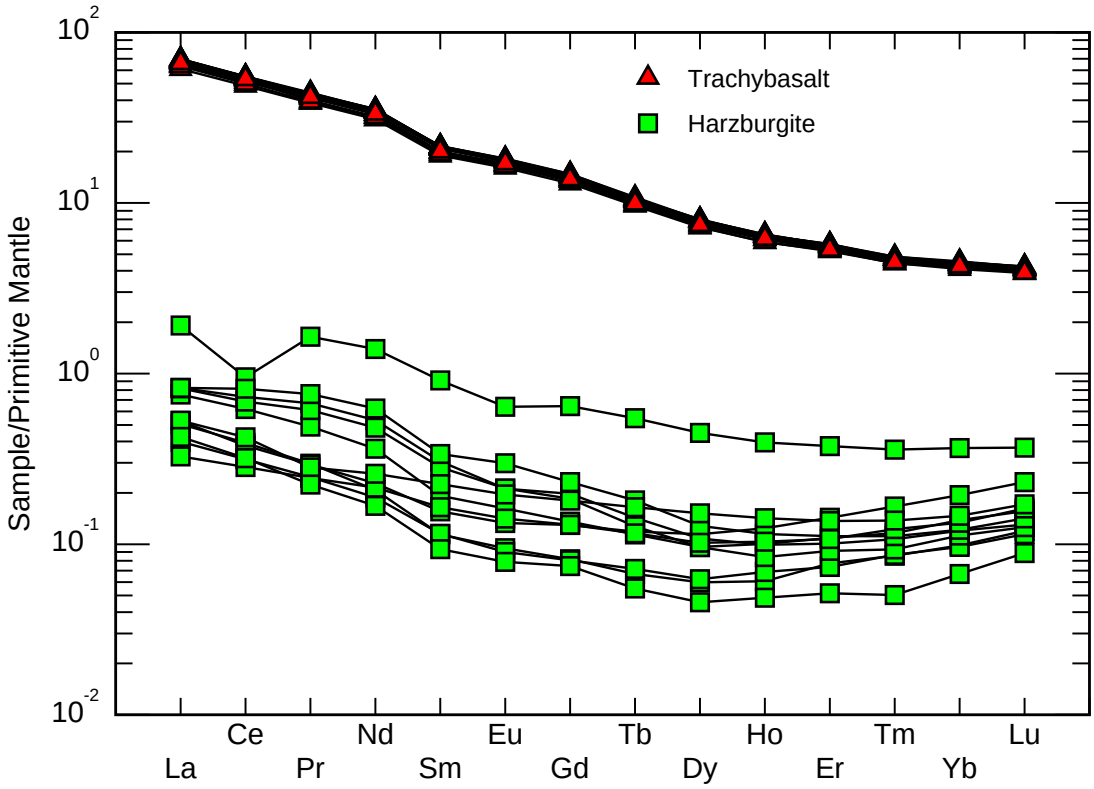

Figure 7: Lorena Butte harzburgite xenoliths and trachybasalts whole-rock REE concentrations. PM normalizations from McDonough and Sun (1995).

Trace element variations in the Lorena Butte harzburgite xenoliths differ significantly from those of abyssal harzburgites (e.g., Day et al., 2017). The Lorena Butte harzburgites generally display near-PM concentrations of incompatible trace elements, whereas abyssal harzburgites are heavily depleted in incompatible trace elements as a result of melt extraction (e.g., Becker & Dale, 2016; Day et al., 2017). The relative enrichment of incompatible trace elements in the Lorena Butte harzburgites compared to the melt-depleted upper mantle can be explained by metasomatic processes involving slab-derived fluids or melts typical within a subduction setting (e.g., Brandon et al., 1996, Downes, 2001).

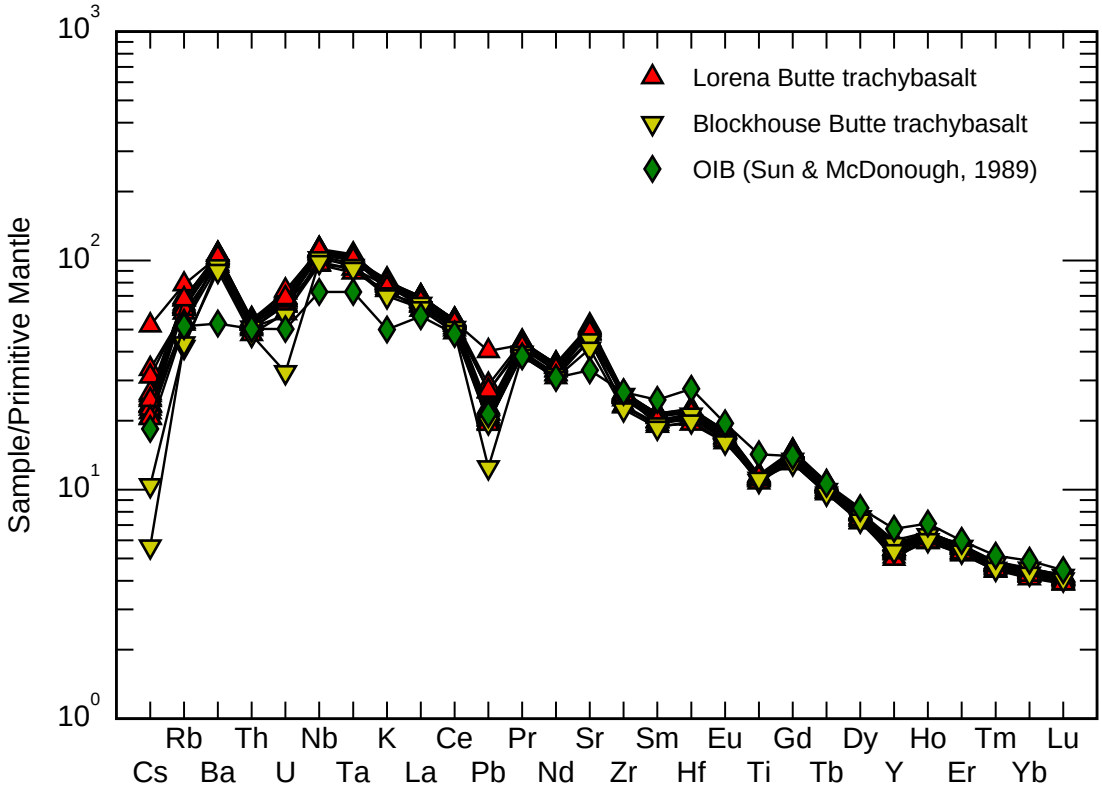

Figure 8: Lorena Butte and Blockhouse Butte trachybasalt whole-rock incompatible trace element concentrations. The trachybasalt trends closely follow the OIB trend after Sun and McDonough (1989). PM normalizations from McDonough and Sun (1995).

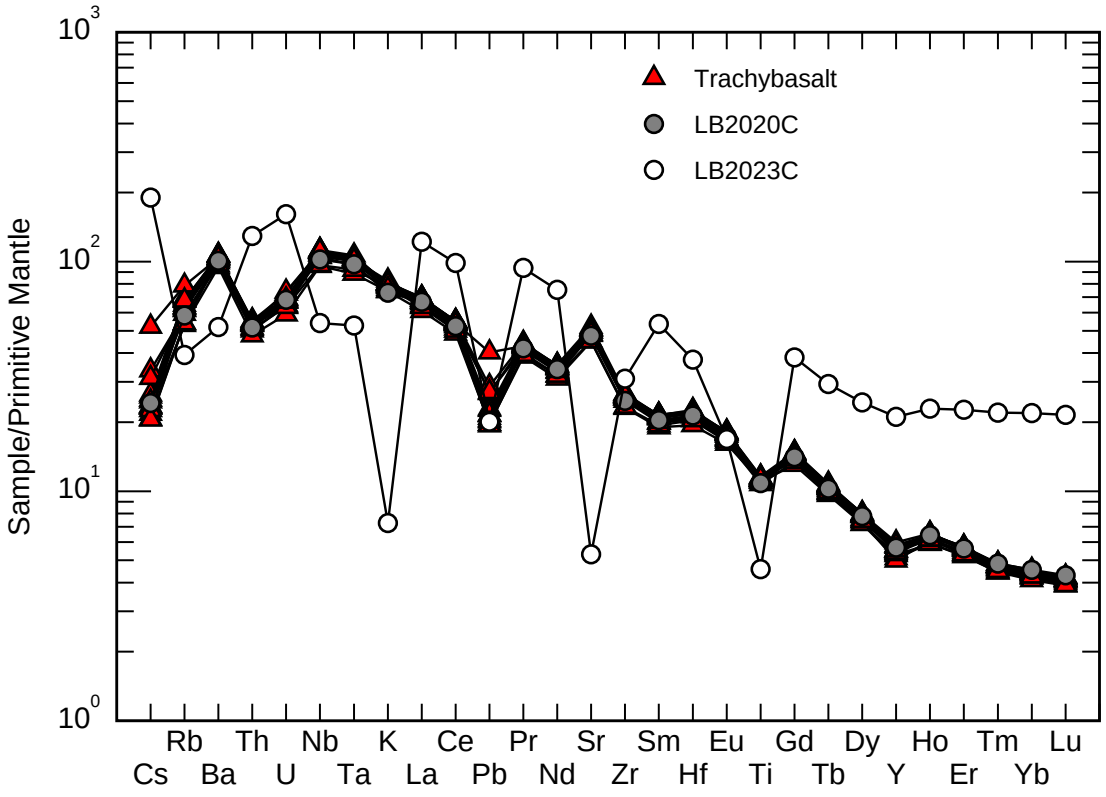

Figure 9: Whole-rock incompatible trace-element concentrations of Lorena Butte crustal xenoliths. Mafic granulite LB2020C follows the same trend as the trachybasalts, while rhyolitic sample LB2023 follows a different trend with variable enrichments or depletion in fluid-mobile elements and elevated REEs. PM normalizations from McDonough and Sun (1995).

For the crustal xenoliths, the incompatible trace element variation of LB2020C mirrors that of the trachybasalts. Sample LB2023C is generally more enriched relative to the lavas with the incompatible trace elements ranging from ~5 × PM to ~200 × PM, except for strong depletions in K, Sr, and Ti, and moderate depletions in Rb, Ba, Nb, Ta, Pb, Zr, and Eu (Figure 9). The REE pattern show a decreasing trend with increasing compatibility from La ~120 × PM to Lu ~20 × PM, with a depletion in Eu (Figure 10).

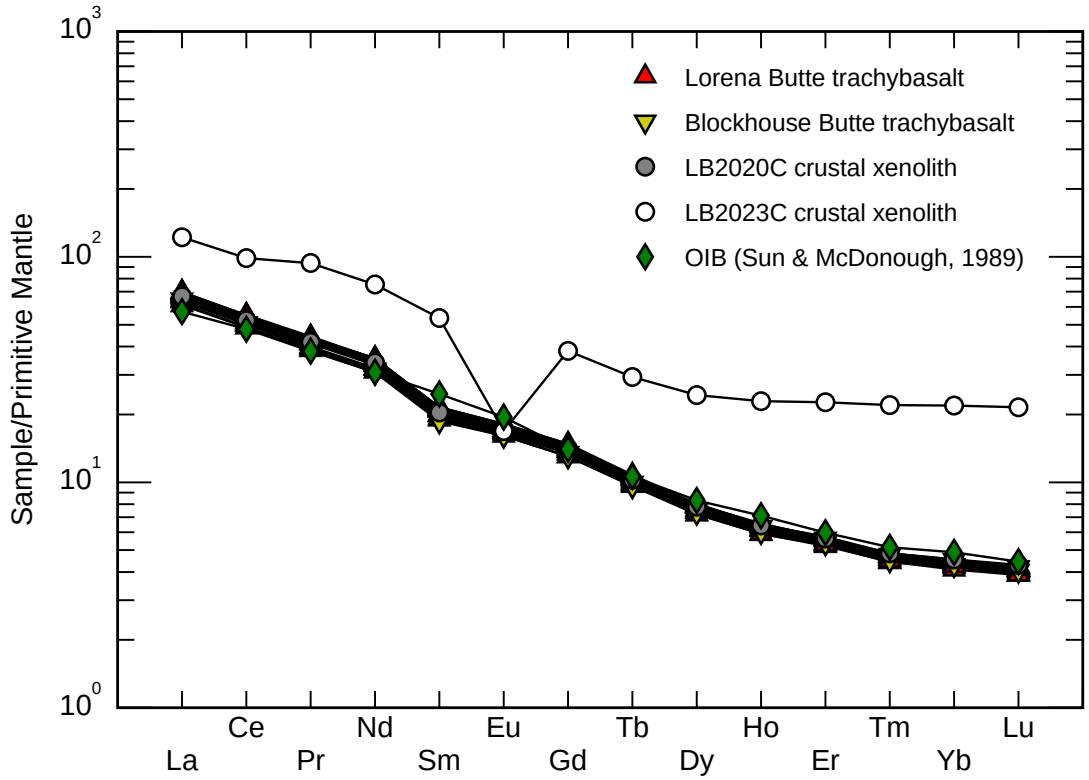

Figure 10: Trachybasalts and crustal xenoliths whole-rock REE concentrations. PM normalizations from McDonough and Sun (1995).

3.3. Highly siderophile element (HSE) abundances and osmium isotope systematics

The HSE (Os, Ir, Ru, Pt, Pd, Re) concentrations and Os isotope systematics of one trachybasalt and 10 harzburgites are reported in Table 3. The trachybasalt has a $^{187}Os/^{188}Os$ of 0.1430 with an Os concentration of 0.017 ppb, which is typical for alkali basalts (e.g., Widom et al., 2003; Day et al., 2010). It displays near-PM concentrations for the relatively incompatible Re and Pd and is moderately depleted (~0.01 × PM) for Pt and the compatible HSE (Os, Ir, Ru).

The $^{187}Os/^{188}Os$ of the harzburgites ranges from 0.1212 to 0.1246 with a mean of 0.1231 (n = 10, 2 SD = 0.0020), which is near the center of the fields for OIB xenoliths (mean = 0.1244) and abyssal peridotites (mean = 0.1243; Becker & Dale, 2016). This average is less radiogenic than the values reported in Brandon et al., 1996, which range from 0.1244 to 0.1304 with a mean of 0.1278 (n = 5, 2 SD

= 0.0043). The $^{187}Re/^{188}Os$ for the samples examined here varies from 0.035 to 1.33, with LB2007X having the highest ratio.

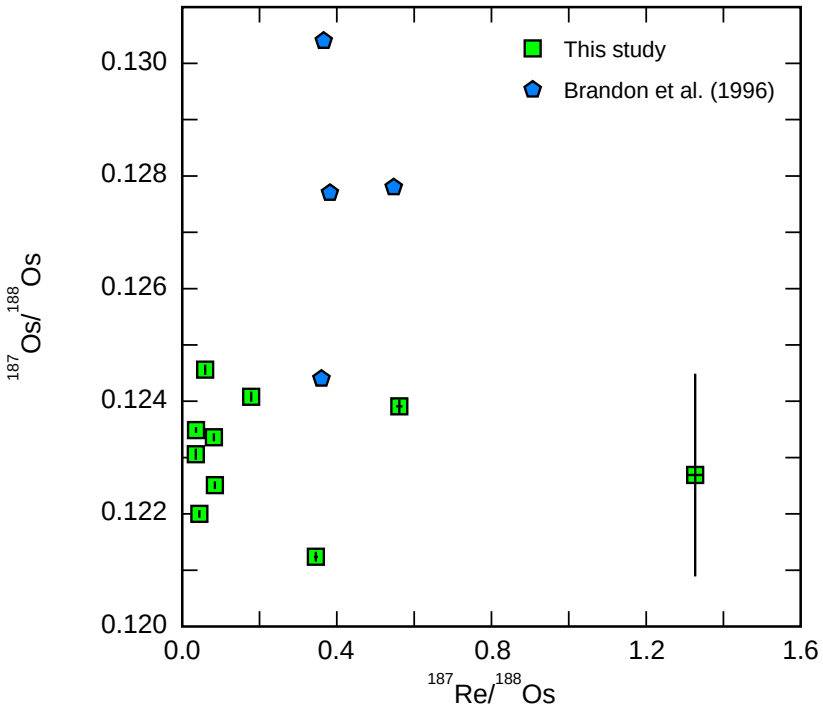

Figure 11: Lorena Butte harzburgite Os isotope systematics. Measured $^{187}Os/^{188}Os$ for this study (green squares) is lower that of Brandon et al. (1996; blue pentagons). Error bars as shown for this study are generally smaller than symbol size, except for $^{187}Os/^{188}Os$ in LB2007X due to a less-than-ideal laboratory run.

The harzburgites exhibit variable concentrations of Os (0.233 to 4.91 ppb), Ir (0.502 to 3.71 ppb), Ru (1.87 to 6.46 ppb), Pt (0.002 to 6.07 ppb), Pd (0.111 to 2.30) and Re (0.030 to 0.083). In general, the PM-normalized HSE trends range from ~0.01 to 1 times PM values and compare favorably to abyssal peridotites except for lower concentrations of the moderately incompatible Re and slightly incompatible Pd in the Lorena Butte harzburgites. Notably, sample LB2007X is highly depleted in Pt (0.0003 × PM).

Variations in the HSE patterns for the peridotites are likely caused by the "nugget effect" resulting from heterogeneous distribution of trace HSE-rich phases in peridotites (e.g., Day et al., 2016). This effect can be reduced if sufficiently large whole-rock samples are prepared and well-mixed. A possible explanation for strong depletion of Pt observed in LB2007X is destabilization of a preexisting Pt-

alloy causing Pt to be released into the melt (Secchiari et al., 2020). This Pt-depletion is observed in some ophiolitic mantle peridotites from New Caledonia (Secchiari et al., 2020) and further suggests heterogeneous fluid flow within the mantle section at a small scale (Snortum & Day, 2020).

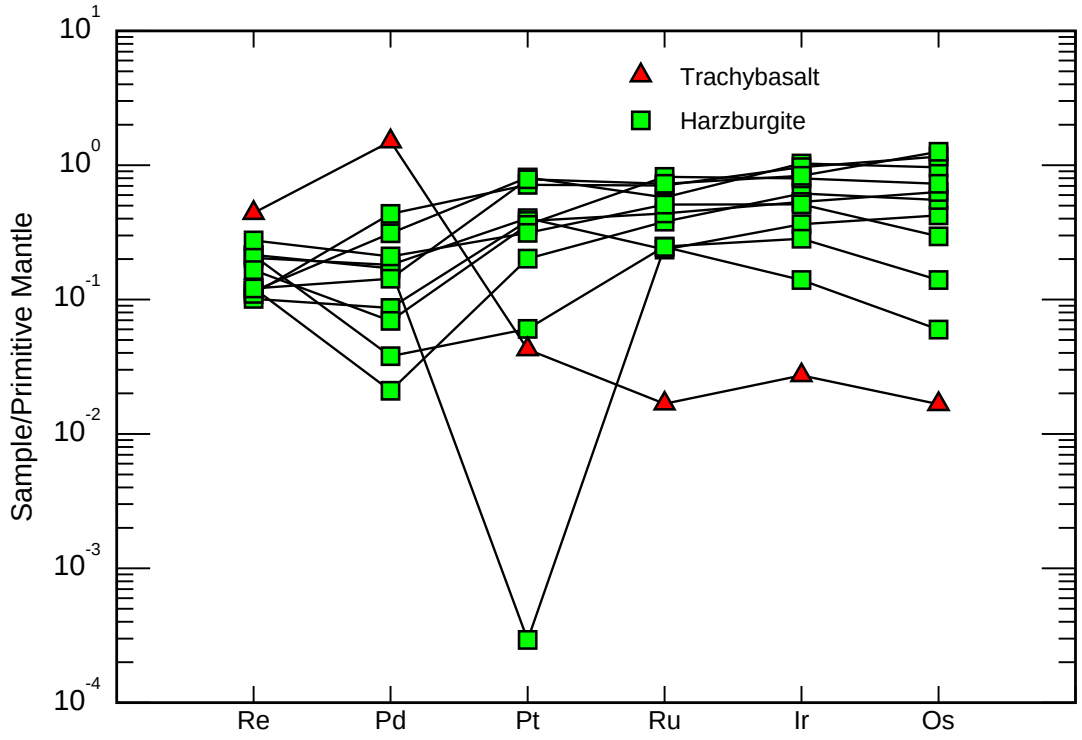

Figure 12: Lorena Butte harzburgites and trachybasalt LB2012 HSE abundances. PM-normalization from Day et al. (2017), with the following PM HSE abundances: 0.3 ppb Re, 5.3 ppb Pd, 7.5 ppb Pt, 7.9 ppb Ru, 3.6 ppb Ir, 3.9 ppb Os.

3.4. Electron probe microanalysis results

The mean microprobe analyses of Lorena Butte harzburgite mineral phases are presented in Table 4. The number of cations per formula unit were determined on a 4-oxygen basis for olivine, 6-oxygen basis for orthopyroxene and clinopyroxene, and 32-oxygen basis for spinel. Olivine and orthopyroxene show very little compositional variations of Fo_{90-91} and En_{89-91}, respectively. Clinopyroxene shows slightly more variation with $Wo_{44-48}En_{48-51}Fs_{4-5}$. For spinel, the Cr-number (defined as Cr/[Cr+Al] × 100) ranges from 28 to 39, corresponding to an estimated 11% to 14% of partial melting (Hellebrand et al., 2001), and the $Fe^{3+}/\Sigma Fe$ ranges from 0.132 to 0.258 (Droop, 1987). These mineral compositions compare favorably

to those reported by Brandon and Draper (1996): $Fo_{90\text{-}93}$ for olivine, En_{90} for orthopyroxene, $Wo_{47}En_{49}Fs_4$ for clinopyroxene, and Cr-number ranging from 32 to 37 in spinels.

3.5. Geothermometry and oxygen fugacity

Equilibrium temperatures for the harzburgite xenoliths were estimated to be between 962 to 1070ºC based on the two-pyroxene geothermometer of Brey and Kohler (1990). The olivine-spinel geothermometer of Jianping et al. (1995) and Ca-in-opx geothermometer of Brey and Kohler (1990) were also used for comparison. Oxygen fugacity (fO_2) was calculated using equation 4 in Davis et al. (2017) following Mattioli and Wood (1988) and Wood and Virgo (1989):

$$\log fO_2 = \frac{-24222}{T} + 8.64 + \frac{0.0567P}{T} - 12\log(1 - \mathrm{Mg\#_{Ol}}) - \frac{2620}{T}(\mathrm{Mg\#_{Ol}})^2 + 3 + 2\log(\alpha_{\mathrm{Fe3O4}}^{\mathrm{Spl}})$$

where P is pressure in bars, T is temperature in Kelvins, $\mathrm{Mg\#_{Ol}}$ is the Mg-number in olivine (Mg-number = Mg/[Mg+Fe]), $X_{\mathrm{Fe}}^{\mathrm{M1}}$ and $X_{\mathrm{Fe}}^{\mathrm{M2}}$ are the mole fractions of Mg and Fe in two orthopyroxene octahedral sites calculated following Wood and Banno (1973), and $\alpha_{\mathrm{Fe3O4}}^{\mathrm{Spl}}$ is the activity of the magnetite component in spinel calculated using the MELTS Supplemental Calculator (Sack & Ghiorso, 1991a, 1991b; https://melts.ofm-research.org/CalcForms/index.html). Pressure is assumed to be 15 kbar, approximately in the middle of the spinel stability field, following Wood et al. (1990) and Brandon and Draper (1996). Calculations of temperature and oxygen fugacity are shown in Table S6.

Oxygen fugacity is reported relative to the fayalite-magnetite-quartz (FMQ) buffer parameterized by Frost (1991):

$$\log fO_2(\mathrm{FMQ}) = \frac{-25096.3}{T} + 8.735 + \frac{0.11(P-1)}{T}$$

Using the Brey and Kohler (1990) two-pyroxene geothermometer, the calculated fO_2 ranges from 0.2 to 1.5 log units above the fayalite-magnetite-quartz buffer (FMQ). The Wood and Virgo (1989) correction procedure for $Fe^{3+}/\Sigma Fe$, which improves the accuracy of the calculations, was not applied

because Mossbauer spectroscopy was not conducted for this study due to time constraints. Hence, the uncertainty is roughly 0.5 log units of fO_2, with calculated temperatures representing the parameter with the largest possible source of error. These values compare favorably to those previously reported by Brandon and Draper (1996) using the two-pyroxene geothermometer of Brey and Kohler (1990) and the fO_2 formulation of Wood and Virgo (1989): 0.3 to 1.4 log units above FMQ, with an uncertainty of 0.4 to 0.5 log units.

Compared to the fO_2 formulation of Wood and Virgo (1989), the fO_2 formulation of Davis et al. (2017) used in this study results in fO_2 values that are approximately 0.3 log units higher (Birner et al., 2018). This is within the uncertainty of the measurement, however, so does not significantly alter the fO_2 estimates.

4. Discussion

4.1. Lorena Butte volcanic stratigraphy and melt chemistry

Rising approximately 100 meters in height above the surrounding topography, Lorena Butte is one of ~25 Pleistocene scoria cones that superimposes a Pliocene shield-like edifice in the southern section of the volcanic field (Figure 13). This edifice consists mostly of mafic flows and vents but has a largely rhyolitic core. The edifice and associated vents extruded through the mid-Miocene Wanapum member of the Columbia River Basalt Group (CRBG; Hildreth & Fierstein, 2015). Previous K-Ar dating yielded ages ranging from 2 Ma to 600 ka across the scoria cones located in the southern section of the volcanic field (Uto et al., 1991; Hildreth & Fierstein, 2015), though no geochronological data have been published for Lorena Butte. A significant portion of the eastern half of Lorena Butte has been quarried for commercial use, exposing minimally weathered scoria, crustal xenoliths, and peridotite xenoliths. Samples were collected stratigraphically upward from near the center of the cone. Approximately 15 meters of vertical section was sampled, limited by safety and accessibility in the quarry. In the section sampled, the strata alternated between scoriaceous tephra containing a high (>40%) proportion and a low (<20%) proportion of 10-cm to 1-m-sized vesiculated bombs. Both strata hosted various xenolith species.

The color of the scoria ranged from brown to dark gray to red moving up section (Figure 14), likely reflecting a change in oxidation near the vent.

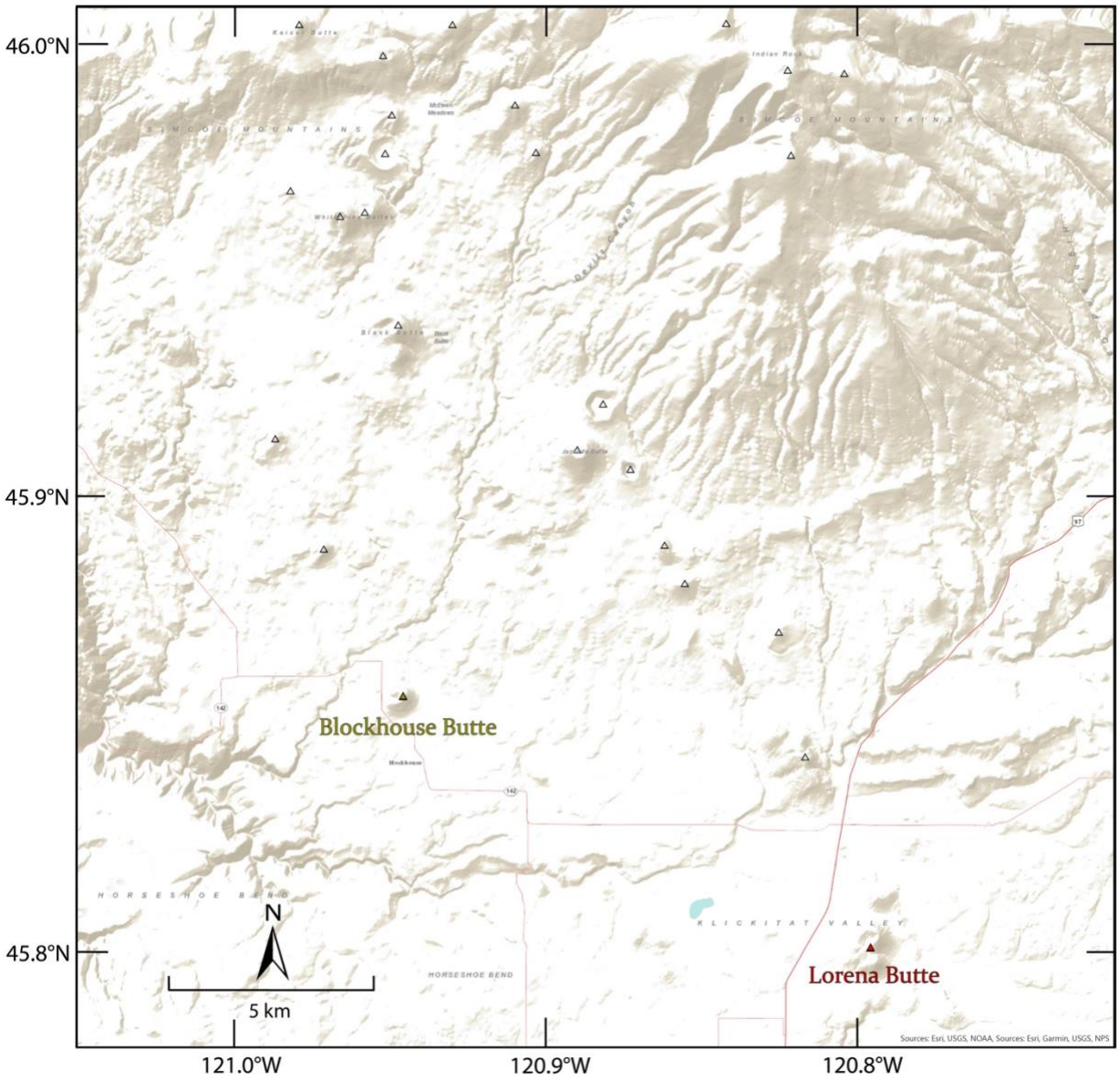

Figure 13: Terrain map of the southern section of Simcoe Mountains volcanic field showing the locations of Lorena Butte and Blockhouse Butte. The shield-like edifice spans the northwestern quarter of the map. Scattered cones and vents likely associated with the shield are marked by triangles.

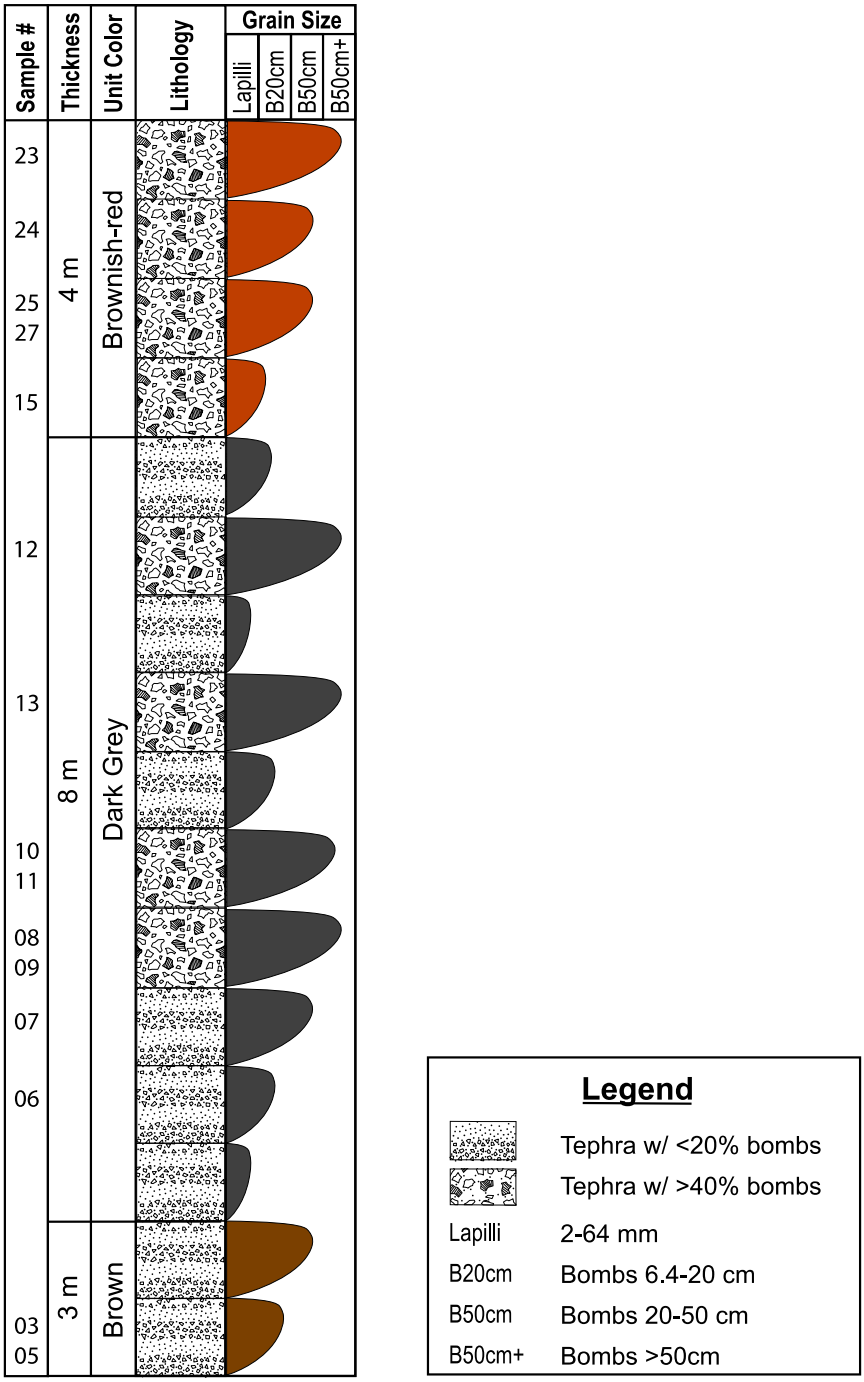

Figure 14: Simplified ~15-meter vertical section of Lorena Butte showing relative stratigraphic positioning of samples. The sample numbers shown are the last two digits of the tephra samples (e.g., sample #23 is LB2023L). Thicknesses of strata are approximate and not to scale.

The alternating strata containing different proportions of volcanic bombs suggest that the vent activity shifted between Hawaiian and Strombolian eruptive styles. However, no significant chemical variation is observed across the studied section of the cone despite changes in stratigraphy. Major- and trace-element trends show no correlation with respect to stratigraphy and display little overall variability between samples except for B, S, Cu, Zn, and Pb, which vary considerably in abundance (1-2 magnitudes) with no observed correlation to stratigraphy or silica content. Furthermore, no chemical distinction is observed between the subset of tephra which hosts harzburgite xenoliths (LB2005L, LB2007L, LB2009L, LB2011L, LB2019L, LB2024L, LB2025L, and LB2027L) and one crustal xenolith (LB2023L) and those which do not host any xenoliths. The unusually high silica content of crustal xenolith LB2032C (82.9 wt. %) suggests that it samples the rhyolitic interior of the Pliocene shield. Mafic granulite xenolith LB2020C has major- and trace-element compositions closely matching that of the trachybasaltic tephra.

The two trachybasalts from Blockhouse Butte display similar major- and trace-element compositions to the Lorena Butte trachybasalts, with trace-element compositions closely following the OIB composition of Sun and McDonough (1989). A comparison of the HSE pattern for the Lorena Butte trachybasalt (LB2012L) with ocean island basalts show that the Lorena Butte melt is more depleted than the Hawaiian lavas (Ireland et al., 2009) in the compatible HSEs due of the high degree of melting experienced by the Hawaiian lavas. Instead, it follows the general pattern of the Cook Island (Snortum et al., 2019) and Canary Island lavas (Day et al., 2010), which have been shown to represent low degrees of partial melting. This suggests that Lorena Butte, Blockhouse Butte, and possibly other lavas in Simcoe sample a similar degree of partial melting and similarly fertile intraplate melt source.

A chemical comparison between Lorena Butte and the Columbia River flood basalts over which the cone lies can provide insight into their magmatic history. Compared with the Steens and Imnaha basalts (Day et al., 2021)—two of the earliest members of the CRBG—the Lorena Butte trachybasalts follow the same general trace-element pattern except for greater enrichment in the most incompatible elements (Figure 15). The Lorena Butte trachybasalt where the HSE were analyzed displays generally

lower HSE content and higher $^{187}Os/^{188}Os$ than the Steens basalts (0.1292 to 0.1336), but has similar HSE contents (Day et al., 2021) and $^{187}Os/^{188}Os$ (0.134 to 0.158; Chesley & Ruiz, 1998) as the Imnaha basalts (Figure 16). Subsequent Grande Ronde and Wanapum members of the CRBG have progressively higher $^{187}Os/^{188}Os$, which has been proposed to be evidence for increased crustal mixing with the upwelling asthenosphere (Chesley & Ruiz, 1998). Since the Lorena Butte HSE and Os isotope systematics follow that of the Imnaha basalts, the magmatic history of Lorena Butte and plausibly that of the Simcoe Mountains volcanic field can be explained by a similar process where crustal material assimilates with upwelling melt as it extrudes to the surface.

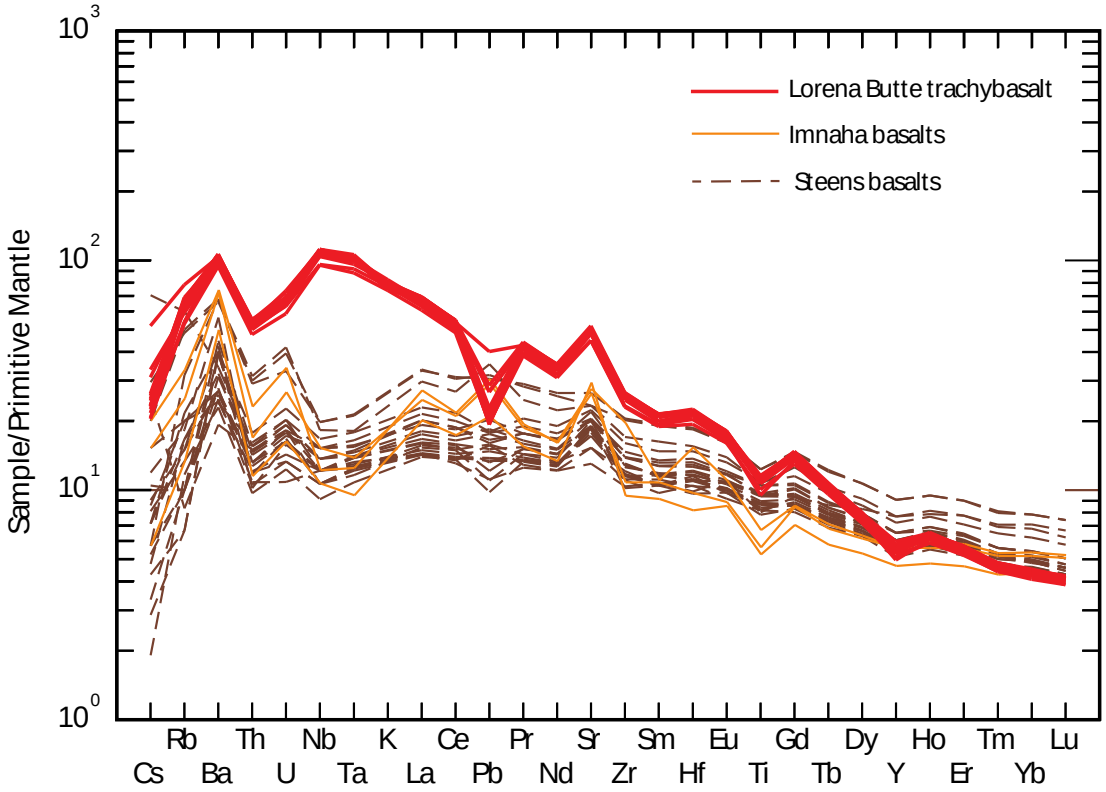

Figure 15: Incompatible trace element trend of the Lorena Butte trachybasalts versus Steens and Imnaha members of the CRBG. The trend of the trachybasalts generally follows that of Steens and Imnaha basalts (from Day et al., 2021) with greater abundances of more incompatible elements, as expected with the higher degree of melting associated with flood-basaltic volcanism. PM normalization after McDonough and Sun (1995).

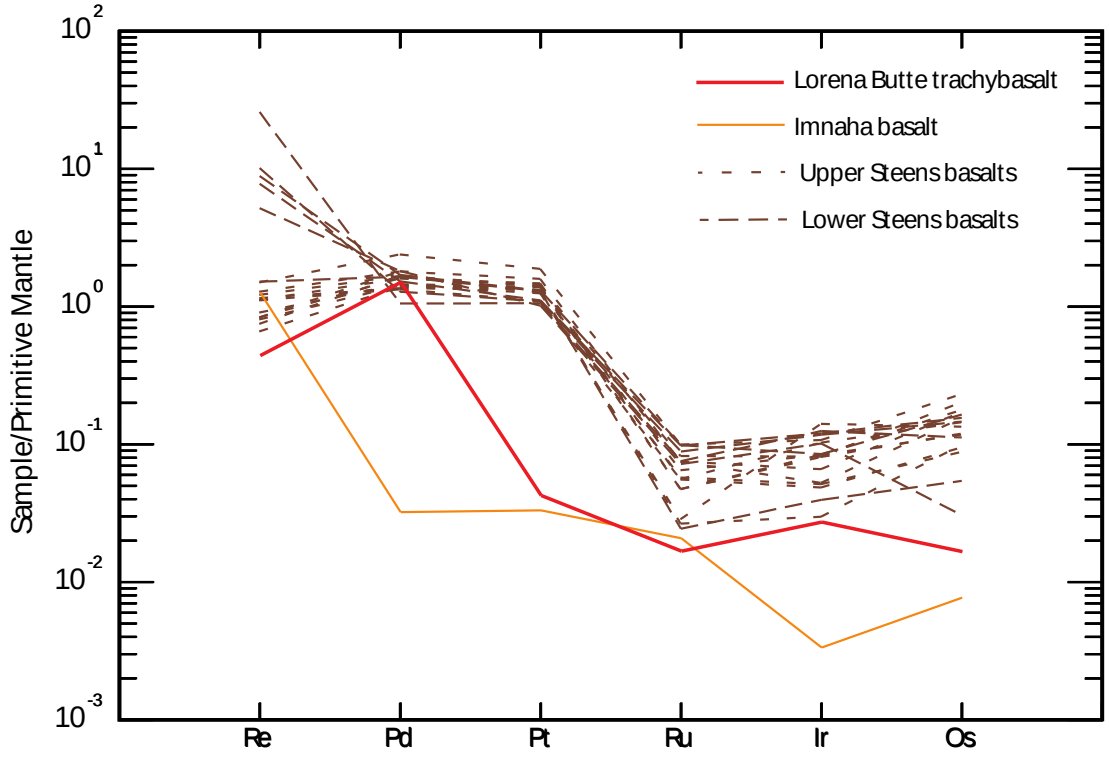

Figure 16: Highly siderophile element content of the Lorena Butte trachybasalt versus the Steens basalts and a single sample of the Imnaha basalts (from Day et al., 2021). Decreasing HSE abundances from Upper Steens, Lower Steens, to Imnaha basalts can be explained by increased mixing with crustal components. The trachybasalt HSE trend generally follows that of the Imnaha basalt, suggesting a similar intermixing of crustal components with an intraplate melt. PM normalization after Day et al. (2017).

4.2 Melt infiltration in the harzburgite xenoliths

Evidence of melt infiltration in the Lorena Butte harzburgite xenoliths is provided by the trends observed in the incompatible trace elements, which generally parallel the trachybasalts but are more depleted (Figure 6). Both the harzburgites and trachybasalts show similar inflections, relative depletions (e.g., Cs, Th, Ti, Y), and relative enrichments (e.g., Ba, Sr). Exceptions include varying degrees of enrichment and depletion of Rb, K, and Pb in the harzburgites. The elevated concentrations of fluid-mobile elements (e.g., Cs, Rb, Ba, U, K, Pb, Na) are broadly similar to serpentinized abyssal peridotites that have been refertilized with seawater (e.g., Frisby et al., 2016). However, the low LOI and lack of visible alternations in the Lorena Butte sample suite suggests refertilization in the sub-arc mantle wedge. Further evidence of melt-refertilization in the harzburgites include elevated concentrations of the LREEs

and high field strength elements (HFSEs: Nb, Ta, Ti, Zr, Hf) relative to what would be expected in melt-depleted residues (Paquet el al., 2021). Correlations observed between the LREEs to HFSEs suggest that the enrichment of both LREEs and HFSEs result from a common magmatic process rather than from serpentinization (Niu, 2004).

The evidence of melt infiltration from the HSE is more limited. Basaltic melts typically have higher Re and Pd content but are one to two magnitudes lower in concentration of the more-compatible HSEs than in mantle peridotites. Thus, the effect of melt infiltration on the HSE in peridotites is observed only at high melt-rock ratios. To illustrate the effects of mixing between the alkali-basaltic melt and the harzburgite xenoliths on Os isotopes, an assumption is made that the trachybasalt (LB2012L) has Os isotope systematics representative of the melt. The melt has more radiogenic $^{187}Os/^{188}Os$ (LB2012L: 0.1430) compared to the harzburgites (mean = 0.1231) but has much lower Os content (LB2012: 0.065 ppb; harzburgites: mean = 2.42 ppb). Thus, melt-rock reactions have limited effects (<2%) on $^{187}Os/^{188}Os$ until a high melt-rock ratio (5:1) is achieved; such a high melt-rock ratio is not observed in the peridotite samples examined here.

4.3. Melt depletion in harzburgite xenoliths

Melt depletion in the harzburgite xenoliths is evidenced by the major element composition, HSE trend, and Os isotope systematics. The high bulk-rock MgO and low Al_2O_3 resembles that of melt-depleted abyssal peridotites (e.g., Day et al., 2017), and Cr-number in spinel grains corresponds to approximately 11% to 14% of partial melting. Additionally, lower-than-PM concentrations of Re and Pd, which behave similarly to moderately incompatible elements during partial melting, provide further evidence for melt depletion.

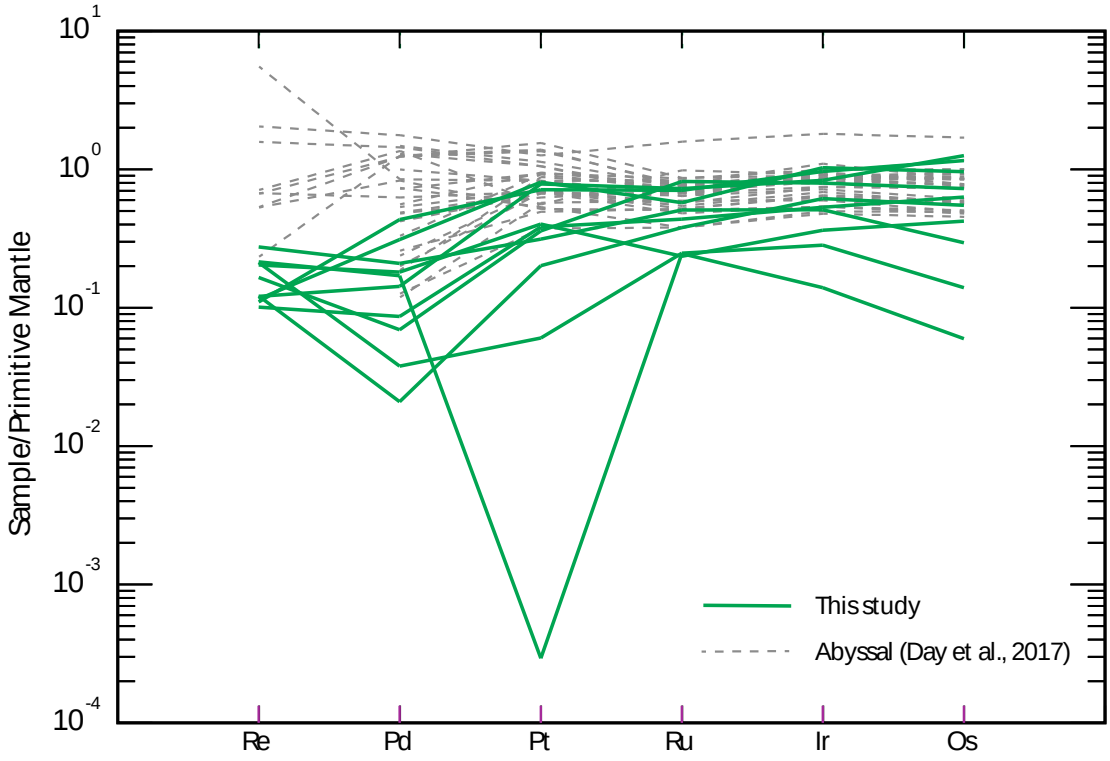

Figure 17: Highly siderophile element content of Lorena Butte harzburgites (green solid lines) and abyssal harzburgites (Day et al., 2017; dashed grey lines). Lorena Butte harzburgites generally follow the trend of abyssal peridotites expect for more depletion in the moderately incompatible Re and slightly incompatible Pd, suggesting similar to slightly greater extents of melt depletion. PM normalization after Day et al. (2017).

Rhenium depletion ages modelled for the harzburgites range from 360 to 850 Ma ($T_{RD} = 1/[1.67 \times 10^{-11}] \times \ln [\{(0.127 - {}^{187}Os/{}^{188}Os_{sample}) / 0.40186\} + 1]$) and represent minimum depletion ages, assuming no ingrowth from ^{187}Re after melt depletion. These ages contrasts with the negative rhenium depletion ages calculated from the Os isotope systematics of Brandon et al. (1996). Instead, they are similar to depletion ages estimated for abyssal peridotites (e.g., Day et al., 2017; Paquet et al., 2021), which suggests that the Lorena Butte harzburgite suite preserve significant pre-existing melt-depletion.

4.4. Oxidation state

The relatively high oxidization state of the Lorena Butte harzburgites calculated for this study ($\Delta \log fO_2 = \text{FMQ} + 1.0 \pm 0.5$, 1 SD) is typical for mantle peridotite xenoliths found in an active or

recently active subduction zone setting (e.g., Wood et al., 1990; Parkinson & Arculus, 1999; Frost & McCammon, 2008). In comparison, estimates of fO_2 recorded in abyssal peridotites are, on average, approximately one to two log units lower, depending on the pressure, thermometer, and fO_2 formulation used (Bryndzia & Wood, 1990; Wood et al., 1990; Birner et al., 2018). This shows that the Lorena Butte harzburgites have likely experienced an increase of oxygen fugacity in the sub-arc mantle lithosphere relative to the depleted MORB mantle represented by abyssal peridotites.

A question arises concerning the nature of the oxidizing agent and the mechanism by which it imposes high oxygen fugacities to the sub-arc mantle. Brandon and Draper (1996) proposed that water transported by a slab-derived fluid or hydrous melt could oxidize the mantle wedge via the dissociation of H_2O into O^{2-} and H_2. This is supported through a mass balance of the flux of water through subduction zones and the amount of water required to impart the high oxidation signature. However, whether water is an effective oxidization agent in the mantle wedge remains controversial (e.g., Frost & Ballhaus, 1998; Kelley & Cottrell, 2009). Despite this controversy, recent thermodynamic modelling has demonstrated that aqueous fluids can effectively oxidize Fe in the sub-arc mantle through the reduction of H^+ to H_2 in the fluid (Iacovino et al., 2020).

Alternatively, sulfur in the fluid or melt have been proposed to be an effective oxidizer (e.g., Kelley & Cottrell, 2009; Klimm et al., 2012). The study of Benard et al. (2018) has shown from glass inclusions in spinel harzburgite xenoliths from the Kamchatka and West Bismarck arcs (Papua New Guinea) that Fe^{2+} is oxidized by S^{6-} in the melt inclusions. These melt inclusions record trace-element ratios and sulfur isotope signatures of subducted serpentines, suggesting that slab-derived sulfur in fluids or melts effectively oxidizes the mantle wedge.

Based on the evidence presented in prior studies, the oxidizing agent in the mantle is plausibly a combination H^+ and S^{6-} in slab-derived fluids or melts. More research is needed to determine the proportion of the oxidizing agents in the fluid or melt in different subduction localities and if other oxidizing species are involved.

4.5. Lorena Butte harzburgites: Origin as mantle residuum below a spreading ridge

The tectonic setting of Lorena Butte in the Cascade back-arc and the moderately high oxidization state of the harzburgite xenoliths suggest that the harzburgites have been influenced by modern arc-related processes. However, the trace-element composition points to an enriched intraplate melt rather than a typical arc magma. Additionally, the Lorena Butte harzburgites generally compare well with abyssal peridotites, which represent the residual mantle after melt extraction beneath mid-ocean ridges (e.g., Dick et al., 1984). This is shown in the major-element content, near-PM HSE trends, and unradiogenic $^{187}Os/^{188}Os$. Rhenium depletion ages of up to 850 Ma records ancient melt depletion, much older than expected given that the initiation of the Cascadia subduction zone occurred at ~45 Ma (du Bray & John, 2011).

A model to explain the data is that the harzburgites originated as mantle residuum from melt extraction below a spreading ridge—analogous to abyssal peridotites—and were then entrained into the mantle wedge below the Cascade arc. One mechanism for this emplacement is that the oceanic lithosphere failed to subduct because of being less dense from high melt depletion. This model has been proposed by Parkinson et al. (1998) in their study of the Izu-Bonin-Mariana forearc peridotites that also record ancient melt depletion. A second, more likely mechanism is that the harzburgites were once part of the shallow mantle below a large oceanic basalt plateau following a hot-spot track, which then accreted onto the North American continental margin. This scenario has been proposed to form the Eocene Siletzia terrane in the coastal region of Oregon and Washington (e.g., Duncan, 1982; Camp et al., 2017). In either case, the depleted peridotite mantle would have been stabilized in the continental margin and become entrapped in the mantle wedge below the Cascade arc, implying that subduction zones can preserve ancient oceanic lithosphere (Parkinson et al., 1998).

Subsequent processes involving the extrusion of the harzburgite xenoliths through intraplate-type volcanism could be explained by deeply seated melts upwelling though a slab window in the subducting lithosphere. This is supported by tomographic models of a slab tear in the subducting Farallon plate developing at ca. 17 Ma (Liu & Stegman, 2012), allowing for decompression melting and the rise of

magmas through the subducting lithosphere. As the formation of this slab tear is contemporaneous with the 16.7 to 15.9 Ma main eruption phase of the Columbia River flood basalts (Kasbohm & Schoene, 2018), it likely led to the onset of the flood-basalt volcanism (Liu & Stegman, 2012; Camp et al., 2017). Later Pliocene-Pleistocene alkali volcanism in the Simcoe Mountains sampled this intraplate melt and entrained the harzburgites in the mantle wedge, carrying the xenoliths to the surface.

5. Conclusions

Comprehensive examination of Lorena Butte harzburgite xenoliths for $^{187}Os/^{188}Os$ and highly siderophile element abundances confirms that they represent a melt-depleted source, suggesting inception in the oceanic mantle lithosphere. These harzburgites have unradiogenic $^{187}Os/^{188}Os$ (0.1212 to 0.1246) representing time of rhenium depletion ages of up to 850 Ma. Substantial evidence for oxidization ($\Delta \log fO_2 = \mathrm{FMQ} + 1.0 \pm 0.5$) by slab-derived fluids or melts in addition to infiltration by intraplate melts show a complicated petrological history for these harzburgites. The melt hosting the xenoliths have also been demonstrated to be similar to the Imnaha member of the Columbia River Basalt Group in terms of $^{187}Os/^{188}Os$ (0.1430) and highly siderophile element abundances, suggesting a related magmatic history. I propose that the Lorena Butte harzburgites originated as mantle residuum in the oceanic lithosphere which has then been emplaced into the mantle wedge below the Cascade arc. Subsequent intraplate volcanism rising through a slab window in the subducting Farallon slab mixed with mantle wedge material and country rock, which is then sampled by the Simcoe Mountains volcanic field. This would indicate that subduction zones can preserve unusually old and melt-depleted mantle derived from a different tectonic setting.

Future work

Peridotite xenoliths hosted in alkali-basaltic melts have been described in several sites besides Lorena Butte throughout the Simcoe Mountains volcanic field (Hildreth & Fierstein, 2015). However, they remain relatively unsampled due to their location on private lands and/or in the Yakama Nations, making access more challenging. Comprehensive chemical analyses of these peridotites may be especially useful to further constrain HSE content and Os isotope systematics in the mantle wedge below the central Cascade arc.

In addition, a geophysical or geodynamical model of emplacement of the oceanic mantle into the mantle wedge could add to my proposal on the origination of the harzburgite xenoliths, or perhaps offer a different perspective of emplacement.

Also, the HSE content of the Columbia River Basalt Group members has remained largely unexplored despite numerous petrological studies. Additional HSE analyses of the CRBG can reveal insights to the melting processes and crust-mantle interactions of the flood basalts as well as their relationship to Simcoe and other volcanic centers in the central Cascades.

Finally, a comprehensive study and comparison of peridotite xenoliths from other active arc settings can add to our understanding of subduction zones. Although mantle peridotites xenoliths from Ichinomegata, Japan, and Kamchatka, Russia, have previously been reported for $^{187}Os/^{188}Os$ (Brandon et al., 1996; Widom et al., 2003), the sample size remains small, and HSE data besides Re and Os are also missing. A more comprehensive dataset in these peridotite xenoliths may prove invaluable to gain a more complete view of HSE behavior and processes occurring in subduction zones on a global scale.

References:

Abbey, S. (1983). Studies in "standard samples" of silicate rocks and minerals, 1969-1982. *Papers - Geological Survey of Canada, 83-15*, 1-114.

Arai, S., & Ishimaru, S. (2007). Insights into petrological characteristics of the lithosphere of mantle wedge beneath arcs through peridotite xenoliths: a review. *Journal of Petrology, 49*(4), 665-695.

Becker, H., & Dale, C. W. (2016). Re–Pt–Os isotopic and highly siderophile element behavior in oceanic and continental mantle tectonites. *Reviews in Mineralogy & Geochemistry, 81*, 369–440.

Bénard, A., Klimm, K., Woodland, A. B., Arculus, R. J., Wilke, M., Botcharnikov, R. E., Shimizu, N., Nebel, O., Rivard, C., & Ionov, D. A. (2018). Oxidising agents in sub-arc mantle melts link slab devolatilisation and arc magmas. *Nature Communications, 9*(3500), 1-10.

Best, M. G. (2003). *Igneous and Metamorphic Petrology, Second Edition*. Blackwell Publishing.

Birck, J. L., Roy Barman, M., & Capmas, F. (1997). Re-Os isotopic measurements at the femtomole level in natural samples. *Geostandards Newsletter, 20*(1), 19-27.

Bird, P. (2003). An updated digital model of plate boundaries. *Geochemistry, Geophysics, Geosystems, 4*(3), 1-52.

Birner, S. K., Cottrell, E., Warren, J. M., Kelley, K. A., & Davis, F. A. (2018). Peridotites and basalts reveal broad congruence between two independent records of mantle fO2 despite local redox heterogeneity. *Earth and Planetary Science Letters, 494*, 172-189.

Boyd, F. R., & Mertzman, S. A. (1987). Composition and structure of the Kaapvaal lithosphere, southern Africa. *Magmatic Processes: Physicochemical Principles: Geochemical Society Special Publications, 1*, 13-24.

Brandon, A. D., & Draper, D. S. (1996). Constraints on the origin of the oxidation state of mantle overlying subduction zones: An example from Simcoe, Washington, USA. *Geochimica et Cosmochimica Acta, 60*(10), 1739-1749.

Brandon, A. D., Creaser, R. A., Shirely, S. B., & Carlson, R. W. (1996). Osmium recycling in subduction zones. *Science, 272*(5263), 861-864.

Brey G. P., & Kohler, T. (1990). Geothermobarometry in four-pahse lherzolites II. New thermobarometers, and practical assessment of existing thermobarometers. *Journal of Petrology, 31*(6), 1353-1378.

Bryndzia, L. T., & Wood, B. J. (1990). Oxygen thermobarometry of abyssal spinel peridotites: The redox state and C–O–H volatile composition of the Earth's sub-oceanic upper mantle. *American Journal of Science, 290*, 1093-1116.

Camp, V. E., Ross, M. E., Duncan, R. A., Kimbrough, D. L. (2017). Uplift, rupture, and rollback of the Farallon slab reflected in volcanic perturbations along the Yellowstone adakite hot spot track. *Journal of Geophysical Research: Solid Earth, 122*(9), 7009-7041.

Chesley, J. T., & Ruiz, J. (1998). Crust-mantle interaction in large igneous provinces: Implications from Re-Os isotope systematics of the Columbia River flood basalts. *Earth and Planetary Science Letters, 154*, 1–11.

Cohen, A. S., & Water, F. G. (1996). Separation of osmium from geological materials by solvent extraction for analysis by thermal ionisation mass spectrometry. *Analytica Chimica Acta, 332*, 269-275.

Davis, F. A., Cottrell, E., Birner, S. K., Warren, J. M., & Lopez, O. G. (2017). Revisiting the electron microprobe method of spinel-olivine-orthopyroxene oxybarometry applied to spinel peridotites. *American Mineralogist, 102*, 421-435.

Day, J. M.D. (2013). Hotspot volcanism and highly siderophile elements. *Chemical Geology, 341*, 50-74.

Day, J. M.D., & Walker, R. J. (2015). Highly siderophile element depletion in the Moon. *Earth and Planetary Science Letters, 423*, 114-124.

Day, J. M.D., Nutt, K. L.R., Mendenhall, B., Peters, B. J. (2021). Temporally variable crustal contributions to primitive mantle-derived Columbia River Basalt Group magmas. *Chemical Geology, 572*.

Day, J. M.D., Pearson, D. G., Macpherson, C. G., Lowry, D., & Carracedo, J. C. (2010). Evidence for distinct proportions of subducted oceanic crust and lithosphere in HIMU-type mantle beneath El Hierro and La Palma, Canary Islands. *Geochimica et Cosmochimica Acta, 74*(22), 6565-6589.

Day, J. M.D., Peters, B. J., & Janney, P. E. (2014). Oxygen isotope systematics of South African olivine melilitites and implications for HIMU mantle reservoirs. *Lithos, 202–203*, 76–84.

Day, J. M.D., Walker, R. J., & Warren, J. M. (2017). 186Os–187Os and highly siderophile element abundance systematics of the mantle revealed by abyssal peridotites and Os-rich alloys. *Geochimica et Cosmochimica Acta, 200*, 232–254.

Day, J. M.D., Waters, C. L., Schaefer, B. F., Walker, R. J., & Turner, S. (2016). Use of hydrofluoric acid desilicification in the determination of highly siderophile element abundances and Re-Pt-Os isotope systematics in mafic-ultramafic rocks. *Geostandards and Geoanalytical Research, 40*(1), 49-65.

Dick, H. J.B., Fisher, R. L., & Bryan, W. B. (1984). Mineralogical variability of the uppermost mantle along mid-ocean ridges. *Earth and Planetary Science Letters, 69*, 88–106.

Downes, G. (2001). Formation and modification of the shallow sub-continental lithospheric mantle: a review of geochemical evidence from ultramafic xenolith suites and tectonically emplaced ultramafic massifs of western and central europe. *Journal of Petrology, 42*(1), 233-250.

Droop, G. T.R. (1987). A general equation for estimating Fe3+ concentrations in ferromagnesian silicates and oxides from microprobe analyses, using stoichiometric criteria. *Mineralogical Magazine, 51*, 431-435.

du Bray, E. A., & John, D. A. (2011). Petrologic, tectonic, and metallogenic evolution of the Ancestral Cascades magmatic arc, Washington, Oregon, and northern California. *Geosphere, 7*(5), 1102-1133.

Duncan, R. A. (1982). A captured island chain in the coast range of Oregon and Washington. *Journal of Geophysical Research, 87*(B13), 10827-10837.

Ertan, I. E., & Leeman, W. P. (1996). Metasomatism of Cascades subarc mantle: Evidence from a rare phlogopite orthopyroxenite xenolith. *Geology, 24*(5), 451-454

Ertan, I. E., & Leeman, W. P. (1999). Fluid inclusions in mantle and lower crustal xenoliths from the Simcoe volcanic field, Washington. *Chemical Geology, 154*, 83-95.

Frisby C., Bizimis M., & Mallick S. (2016) Seawater-derived rare earth element addition to abyssal peridotites during serpentinization. *Lithos, 248-251*, 432–454.

Frost, B. R. (1991). Introduction to oxygen fugacity and its petrologic importance. *Reviews in Mineralogy and Geochemistry, 25*, 1-9.

Frost, B. R., & Ballhaus, C. (1998). A comment on ‘‘Constraints on the origin of the oxidation state of mantle overlying subduction zones: An example from Simcoe, Washington, USA.’’ Geochimicha et Cosmochimica Acta, *62*(2), 329–331

Frost, D. J., & McCammon, C. A. (2008). The redox state of Earth's mantle. *Annual Reviews of Earth and Planetary Sciences, 36*, 389-420.

Govindaraju, K. (1994). Compilation of working values and sample description for 383 geostandards. *Journal of Geostandards and Geoanalysis, 18*, 158.

Grove, T. L., Chatterjee, N., Parman, S. W., Médard, E. (2006). The influence of H2O on mantle wedge melting. *Earth and Planetary Science Letters, 249*(1–2), 74-89.

Hellebrand, E., Snow, J. E., Dick, D. H., & Hofmann, A. W. (2001). Coupled major and trace elements as indicators of the extent of melting in mid-ocean-ridge peridotites. *Nature, 410*, 677–681.

Hildreth, W., & Fierstein, J. (2015). *Geologic Map of the Simcoe Mountains Volcanic Field, Main Central Segment, Yakama Nation, Washington.* U.S. Geological Survey.

Iacovino, K., Guild, M. R., & Till, C. B. (2020). Aqueous fluids are effective oxidizing agents of the mantle in subduction zones. *Contributions to Mineralogy and Petrology, 175*(36), 1-21.

Ireland, T. J., Walker, R. J., & Garcia, M. O. (2009). Highly siderophile element and 187Os isotope systematics of Hawaiian picrites: Implications for parental melt composition and source heterogeneity. *Chemical Geology, 260*, 112-128.

Jianping, L., Kornprobst, J., Vielzeuf, D., & Fabries, J. (1995). An improved experimental calibration of the olivine-spinel geothermometer. *Chinese Journal of Geochemistry, 14*(1), 68-77.

Kasbohm, J. & Schoene, B. (2018). Rapid eruption of the Columbia River flood basalt and correlation with the mid-Miocene climate optimum. *Science Advances, 4*(9), 1-8.

Kelley, K. A., & Cottrell, E. (2009). Water and the oxidation state of subduction zone magmas. *Science, 325*(5940), 605-607.

Klimm, K., Kohn, S. C., & Botcharnikov, R. E. (2012). The dissolution mechanism of sulphur in hydrous silicate melts. II: Solubility and speciation of sulphur in hydrous silicate melts as a function of fO2. *Chemical Geology, 322–323*, 250-267,

Leeman, W. P., Smith, D. R., Hildreth, W., Palacz, Z., & Rogers, N. (1990). Compositional diversity of late Cenozoic basalts in a transect across the southern Washington Cascades: Implications for subduction zone magmatism. *Journal of Geophysical Reseach, 95*(B12), 19561-19582.

Liu L., & Stegman, D. R. (2012). Origin of Columbia River flood basalt controlled by propagating rupture of the Farallon slab. *Nature, 482*(7385), 386-389.

Luguet A., & Reisberg, L. (2016). Highly siderophile element and 187Os signatures in non-cratonic basalt-hosted peridotite xenoliths: Unravelling the origin and evolution of the post-Archean lithospheric mantle. *Reviews in Mineraology & Geochemistry, 81*(1), 305-367.

Mattioli, G. S., & Wood, B. J. (1988). Magnetite activities across the MgAl2O4-Fe3O4 spinel join, with application to thermobarometric estimates of upper mantle oxygen fugacity. *Contributions to Mineralogy and Petrology, 98*, 148-162.

McDonough, W. F., & Sun, S.-s. (1995). The composition of the Earth. *Chemical Geology, 120*, 223-253.

Mertzman, S. A. (2000). K-Ar results from the southern Oregon-northern California Cascade Range. *Oregon Geology, 62*(4), 99-102.

Niu, Y. (2004). Bulk-rock major and trace element compositions of abyssal peridotites: Implications for mantle melting, melt extraction and post-melting processes beneath mid-ocean ridges. *Journal of Petrology, 45*(12), 2423–2458.

Paquet, M., Day, J. M.D., Brown, D. B., Waters, C. L. (2021). Effective global mixing of the highly siderophile elements into Earth's mantle inferred from oceanic abyssal peridotites. *Geochimica et Cosmochimica Acta*.

Parkinson, I. J., & Arculus, R. J. (1999). The redox state of subduction zones: insights from arc-peridotites. *Chemical Geology, 160*(4), 409- 423.

Parkinson, I. J., Hawkesworth, C. J., & Cohen, A. S. (1998). Ancient mantle in a modern arc: osmium isotopes in Izu-Bonin-Mariana forearc peridotites. *Science, 281*(5385), 2011-2013.

Peacock, S. A. (1990). Fluid processes in subduction zones. *Science, 248*(4953), 329-337

Pearce, J.A. (1983). Role of the sub-continental lithosphere in magma genesis at active continental margins. In C. J. Hawkesworth, M. J. Norry (Eds.), *Continental basalts and mantle xenoliths*, (pp. 230-249). Shiva Publishing Ltd.

Pisut, D. (2020). *Tectonic Plates and Boundaries*. ArcGIS Online. https://www.arcgis.com/home/item.html?id=5113817f8b00453494fd5cf64c099ef9

Sack, R. O., & Ghiorso, M. S. (1991a). An internally consistent model for the thermodynamic properties of Fe-Mg-titanomagnetite-aluminate spinels. *Contributions to Mineralogy and Petrology, 106*, 474-505.

Sack, R. O., & Ghiorso, M. S. (1991b). Chromian spinels as petrogenetic indicators; thermodynamics and petrological applications. *American Minerologist, 76*, 827-847.

Secchiari, A., Gleissner, P., Li, C., Goncharov, A., Milke, A., Becker, H., Bosch, D., Montanini, A. (2020). Highly siderophile and chalcophile element behaviour in abyssal-type and supra-subduction zone mantle: New insights from the New Caledonia ophiolite. *Lithos, 354-355*.

Snortum, E., & Day, J. M.D. (2020). Forearc origin for Coast Range Ophiolites inferred from osmium isotopes and highly siderophile elements. *Chemical Geology, 550*.

Snortum, E., Day, J. M.D., & Jackson, M. G. (2019). Pacific lithosphere evolution inferred from Aitutaki mantle xenoliths. *Journal of Petrology, 60*(9), 1753–1772.

Sun, S.-s., & McDonough, W. F. (1989). Chemical and isotopic systematics of oceanic basalts: implications for mantle composition and processes. *Geological Society, London, Special Publications, 42*(1), 313-345.

Uto, K., Hildreth, W., & Lanphere, M. (1991). Geology, geochemistry and geochronology of the southern half of the Simcoe Mountains volcanic field, Washington. *Eos, Transactions of American Geophysical Union, 72*, 521.

Walker, R. J. (2016). Siderophile elements in tracing planetary formation and evolution. *Geochemical Perspectives, 5*(1), 1-145.

Widom, E., Kepezhinskas, P., & Defant, M. (2003). The nature of metasomatism in the sub-arc mantle wedge: evidence from Re–Os isotopes in Kamchatka peridotite xenoliths. *Chemical Geology, 196*(1-4), 283-306.

Wood, B. J., & Banno, S. (1973). Garnet-orthopyroxene and orthopyroxene-clinopyroxene relationships in simple and complex systems. *Contributions to Mineralogy and Petrology, 42*, 109-124.

Wood, B. J., & Virgo, D. (1989). Upper mantle oxidation state: Ferric iron contents of lherzolite spinels by 57Fe Mössbauer spectroscopy and resultant oxygen fugacities. *Geochimica et Cosmochimica Acta, 53*, 1277–1291.

Wood, B. J., Bryndzia, L. T., & Johnson, K. E. (1990). Mantle oxidation state and its relationship to tectonic environment and fluid speciation. *Science, 248*(4953), 337-345.